Ore Geology Reviews 145 (2022) 104920

Contents lists available at ScienceDirect

Ore Geology Reviews

journal homepage: www.elsevier.com/locate/oregeorev

Petrogenesis of the quartz diorite from the Lietinggang-Leqingla Pb-Zn-Fe-Cu-(Mo) deposit in southern Tibet: Implications for the genesis of a skarn-type polymetallic deposit in the Tibetan-Himalayan collisional orogen

Wang Ma [a,b], Yingchao Liu [b,*], Zhusen Yang [c], Jan Marten Huizenga [d,e,f], Zhenqing Li [c], Miao Zhao [c], Longlong Yue [b], Sibo Zhao [b]

[a] School of Earth Sciences and Resources, China University of Geosciences, Beijing 100083, China
[b] Key Laboratory of Deep-Earth Dynamics of Ministry of Natural Resources, Institute of Geology, Chinese Academy of Geological Sciences, Beijing 100037, China
[c] Key Laboratory of Metallogeny and Mineral Assessment, Institute of Mineral Resources, Chinese Academy of Geological Sciences, Beijing 100037, China
[d] Faculty of Environmental Sciences and Natural Resource Management, Norwegian University of Life Sciences, P.O. Box 5003, NO-1432, Ås, Norway
[e] Economic Geology Research Centre (EGRU), College of Science and Engineering, James Cook University, Townsville, Queensland 4811, Australia
[f] Department of Geology, University of Johannesburg, PO Box 524, Auckland Park, South Africa

ARTICLE INFO

Keywords:
Quartz diorite
Petrogenesis
Lietinggang-Leqingla deposit
Genesis of skarn-type polymetallic deposit
Lhasa terrane

ABSTRACT

The Lietinggang-Leqingla deposit is a representative skarn-type polymetallic deposit in the eastern of the central Lhasa subterrane. It comprises Pb-Zn and Fe-Cu-(Mo) mineralization that are part of the same metallogenic system. Garnet-skarn hosting Fe-Cu-(Mo) mineralization distributed in the contact zone between the Jubuzhari complex intrusions and carbonate strata of the Mengla Formation. The Pb-Zn mineralization is hosted in distal garnet-pyroxene and pyroxene-actinolite skarns, which formed in the strata of Mengla Formation. Here, we investigate quartz diorites (61.06 ± 0.93 Ma) that are related to Fe-Cu mineralization in the northern part of the mining area. The quartz diorites are characterized by low SiO_2 (61.57–65.88 wt%), low K_2O (2.53–3.07 wt%), and high total alkali ($Na_2O + K_2O$) contents (5.69–6.35 wt%). They are enriched in large-ion lithophile elements and light rare earth elements, but depleted in high field strength elements and heavy rare earth elements. The quartz diorites yield variably low $(La/Yb)_N$ ratios (4.29–7.07, the average value is 6.36) with moderately negative Eu anomalies (Eu/Eu* = 0.49–0.72). Furthermore, they exhibit a narrow range in $(^{87}Sr/^{86}Sr)_i$ ratios (0.706355–0.706807) and weakly negative ε_{Nd} (t) (−2.08 to −1.57), and positive ε_{Hf} (t) (+0.14 to +3.46) values. Based on the geochemical characteristics presented in this study and previously published data, we propose that the ore-forming rocks related to Fe-Cu and Pb-Zn mineralization were formed at the same time. The intermediate intrusions associated with Fe-Cu mineralization were derived from partial melting of lithospheric mantle mixed with the rejuvenated lower crustal melts, after which the mixed magma underwent minor fractional crystallization during upwelling. The felsic intrusions associated with Pb-Zn mineralization were formed by melting of mantle-derived basaltic magmas with old lower crust component contributions and which underwent extensive fractional crystallization.

1. Introduction

Skarn deposits are widely distributed around the world and are directly related to magmatic-hydrothermal activity associated with plutonic bodies. Those magmatic fluids are significant sources of economic metals such as iron, copper, gold, molybdenum, tungsten, tin, zinc, and lead (Meinert, 2005). Researchers have studied a variety of topics regarding skarn-type deposits in the past, including tectonic setting, mineral assemblages, geochronology, alteration and mineralization, ore-forming fluids, and the sources of the ore-forming materials (Einaudi et al., 1981, 1982; Newberry and Swanson, 1986; Meinert, 1995, 2005; Samson et al., 2008; Wang et al., 2011; Zarasvandi et al.,

* Corresponding author at: Institute of Geology, Chinese Academy of Geological Sciences, No. 26, Baiwanzhuang Street, Xicheng District, Beijing 100037, China.
E-mail address: lychappy@126.com (Y. Liu).

https://doi.org/10.1016/j.oregeorev.2022.104920
Received 14 December 2021; Received in revised form 26 April 2022; Accepted 29 April 2022
Available online 4 May 2022

2015; Shu et al., 2017; Zhao et al., 2017; Ma et al., 2017, 2019).

It has been demonstrated that the iron ore skarn-type deposits can be related to intermediate-acid igneous rocks such as (quartz) diorite and granodiorite (Li et al., 2012). Copper-zinc-lead skarn ore deposits, on the other hand, are generally associated with I-type granitoids such as monzogranite, granodiorite, and quartz monzonite-porphyry (Hezarkhhani, 2006; Maher, 2010; Kloppenburg et al., 2012). The metal associations are to a large extend controlled by the magma redox state and the degree of fractionation (Chang et al., 2019). In addition, the mantle and crustal materials play an important role in the formation of magmatic hydrothermal deposits (Richard, 2009, 2011; Wang et al., 2015; Yang et al., 2016; Zhang et al., 2019; Xu et al., 2021a).

The Himalayan-Tibetan orogeny resulted from the collision of Indian and Asian continents in the Early Tertiary, resulting in the thickest crust on earth (Yin and Harrison, 2000; DeCelles et al., 2004; Chu et al., 2006; Zhu et al., 2009; Hou et al., 2009, 2015). During the syn-collisional stage (65–41 Ma), asthenospheric upwelling not only promoted partial melting of lithospheric mantle and crust, but also affected the Precambrian basement and Paleozoic sedimentary cover (Hou et al., 2006, 2015, 2021; Zhu et al., 2013), which resulted in the formation of the northern Gangdese Pb-Zn-Ag-Fe-Cu-Mo-W polymetallic belt (NGPB) (Zheng et al., 2015; Fu et al., 2017; Zhang et al., 2019). This belt extends for nearly 600 km along the Luobadui-Milashan Fault in the central Lhasa subterrane (Meng et al., 2007; Huang et al., 2012; Zhao et al., 2014; Zheng et al., 2015; Fu et al., 2017). There are four major types of mineralization systems in the NGPB, including: skarn Fe-(Cu), granite-related Pb-Zn-Ag, skarn Pb-Zn-Fe-Cu-Mo, and porphyry/skarn Mo-Cu-W (Hou et al., 2015; Zheng et al., 2015; Zhang et al., 2019). Previous studies have suggested that the skarn Fe-(Cu) mineralization is associated with syn-collisional metaluminous granodiorites, monzogranites, and quartz diorite, all of which were generated from partial melting of lithospheric mantle mixed with rejuvenated lower crustal melts (Zheng et al., 2015). The ore-forming intrusions related to the skarn Pb-Zn deposits were closely associated with the ancient basement of the central Lhasa subterrane (Fu et al., 2017). The polymetallic deposits that have been found in the NGPB include the Bangpu porphyry/skarn Mo-Cu-Pb-Zn deposit (Zhao et al., 2015), the Longmala skarn Fe-(Cu)-Pb-Zn deposit (Fu et al., 2014), and the Lietinggang-Leqingla Pb-Zn-Fe-Cu-(Mo) deposit (Ma et al., 2015, 2017). These deposits have been well documented in terms of their metallogeny, geochronology, source of ore-forming rocks, and geodynamic setting (Fu et al., 2014; Ma et al., 2015, 2019, 2020; Zhao et al., 2015; Wang et al., 2017, 2018). However, a critical issue that has not been resolved yet is how Pb, Zn, Fe, and Cu metals that are derived from different origin sources can be the enriched together in the same metallogenic system.

The Lietinggang-Leqingla deposit is a skarn-type polymetallic deposit in the NGPB comprising both Pb-Zn and Fe-Cu-(Mo) mineralization. The relationship between the Pb-Zn and the Fe-Cu mineralization, and the different ore-forming intrusions have not been investigated yet. In this paper we present zircon geochronological and Hf isotope, and whole-rock geochemical (major and trace element geochemistry, Sr-Nd isotope) data of the quartz diorite associated with Fe-Cu mineralization from the Lietinggang-Leqingla deposit. We aim to obtain a better understanding of why the skarn-type Pb-Zn and Fe-Cu mineralizations developed in the same metallogenic system.

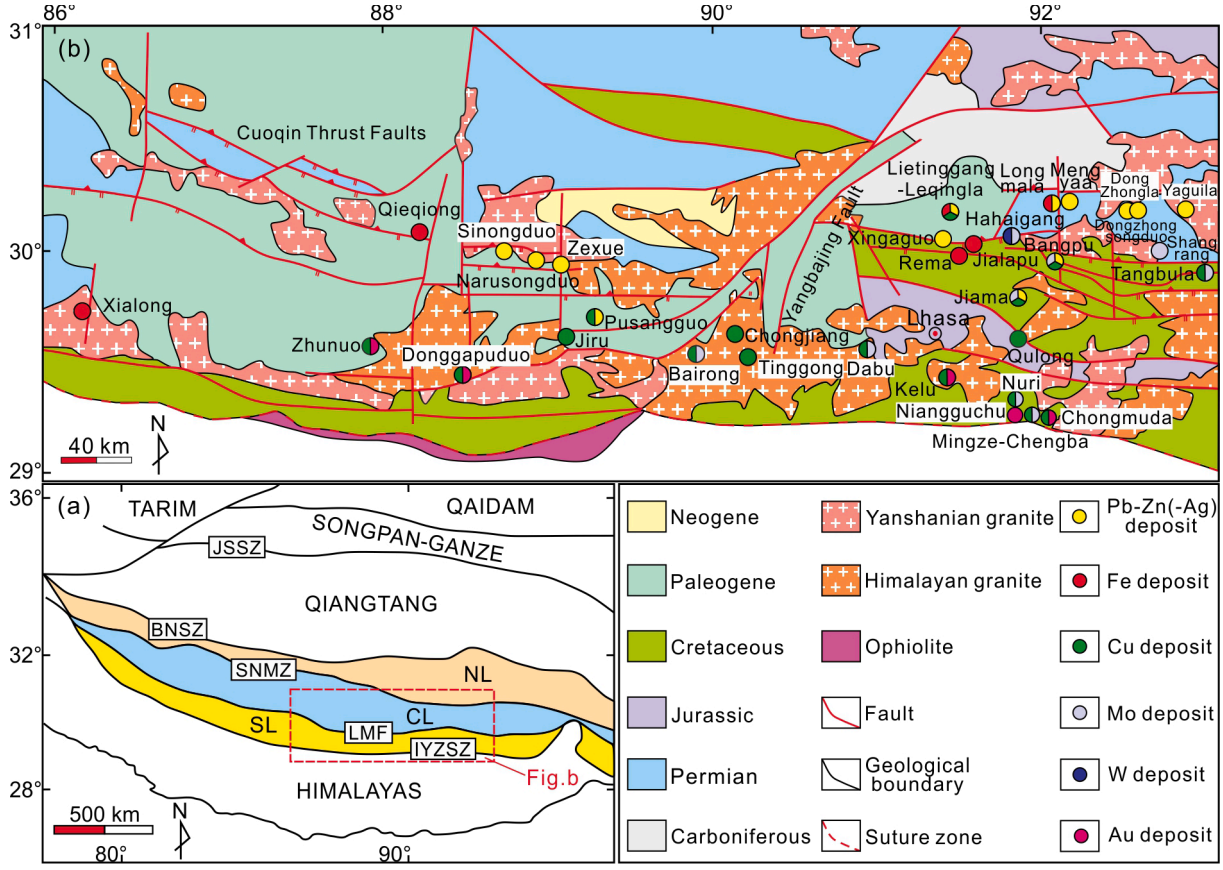

Fig. 1. (a) Geological sketch map of Tibetan Plateau (modified from Zhu et al., 2011); (b) Simplified regional geological map of the central and eastern Gangdese metallogenic belt in the Lhasa terrane showing the distribution of significant ore deposits (modified from Hou et al., 2006; Meng et al., 2007). JSS: Jinsha suture zone; BNS: Bangong-Nujiang suture zone, SNMZ: Shiquan River-Nam Tso Mélange Zone, LMF: Luobadui-Milashan fault, IYZS: Indus-Yarlung Zangbo suture zone, NL: Northern Lhasa subterrane, CL: Central Lhasa subterrane, SL: Southern Lhasa subterrane.

2. Regional geological setting

The Himalayan-Tibetan Plateau is a complex tectonic collage composed of four continental terranes, including (from north to south) the Songpan-Ganze, Qiangtang, Lhasa and Himalayan terranes, which are separated from each other by the Jinsha suture zone (JSSZ), Bangong-Nujiang suture zone (BNSZ), and Indus-Yarlung Zangbo suture zone (IYZSZ), respectively (Yin and Harrison, 2000; Pan et al., 2004; Zhu et al., 2009, 2012) (Fig. 1a). The southernmost Eurasian Lhasa terrane has a length of ~2000 km and a width of 100–300 km. It is bounded to the north by the Bangong-Nujiang suture zone, which was formed by the Late Jurassic-Early Cretaceous closure of the Paleo-Tethyan Ocean due to continental collision between the Lhasa and Qiangtang terranes (Yin and Harrison, 2000; Zhu et al., 2009). To the south, it is bounded by the Indus-Yarlung Zangbo suture zone, which resulted from the Paleocene collision between the Asian and the northward moving Indian continental plates (Mo et al., 2005; Hou et al., 2006). The Lhasa terrane can be further subdivided into a northern, central, and southern subterrane, which are separated by the Shiquan River-Nam Tso Mélange Zone (SNMZ) and the Luobadui-Milashan Fault (LMF), respectively (Fig. 1a; Zhu et al., 2011). The northern Lhasa subterrane comprises Jurassic-Cretaceous and minor Triassic sedimentary rocks and Lower Cretaceous volcano-sedimentary rocks (Pan et al., 2004; Zhu et al., 2011). The central Lhasa subterrane was once a ribbon-shaped microcontinent with a Proterozoic and Archean basement, and comprises widespread Permo-Carboniferous metasedimentary rocks, Late Jurassic-Early Cretaceous volcano-sedimentary rocks, and minor Ordovician, Silurian and Triassic limestones (Pan et al., 2004; Zhu et al., 2010, 2011, 2013). In the southern Lhasa subterrane, the Precambrian crystalline basement is locally preserved (Dong et al., 2010), whereas the sedimentary cover is largely confined to the eastern part, largely consisting of Late Triassic-Cretaceous clastic sedimentary rocks and abundant volcanic rocks collectively known as the Yeba Formation (Pan et al., 2004; Zhu et al., 2008, 2013).

The Lhasa terrane is characterized by the widespread occurrence of Late Triassic-Early Tertiary Gangdese batholiths and the Mesozoic-Cenozoic volcanic successions (i.e., the well-known Gangdese magmatic belt) situated along the southern margin of the Lhasa terrane (Harris et al., 1990; Hou et al., 2015; Mo et al., 2003; Chu et al., 2006; Ji et al., 2009; Zhu et al., 2011, 2013). The formation of these magmatic rocks is related to the subduction of the Neo-Tethyan Ocean and the collision between the Indian and Asian continents (Mo et al., 2005; Ji et al., 2009; Zhu et al., 2009, 2011). The Gangdese magmatic arc records a long, punctuated history of magmatism from ~215 to ~10 Ma, with four periods of intense magmatic activity, i.e., at 210–170 Ma, 110–80 Ma, 65–41 Ma, and 30–10 Ma (Chu et al., 2006; Mo et al., 2007; Ji et al., 2009; Zhu et al., 2017). Intense magmatic activity took place during the Paleocene-Eocene, with the magmatic peak activity at ca. 52 Ma (Zhu et al., 2017). Magmatism during 65–41 Ma associated with the Indian-Asian continental collision and roll-back of the Neo-Tethyan oceanic slab, is characterized by the formation of voluminous arc batholiths and the Linzizong volcanic successions in the south of Tibet (Chung et al., 2005; Hou et al., 2006; Mo et al., 2005, 2007; Zhu et al., 2009, 2011). The arc batholiths comprise Paleocene syn-collisional granitoids, Eocene gabbro and associated granitoid intrusions, and basaltic subvolcanic rocks (Hou and Cook, 2009). The Linzizong volcanic successions (60–42 Ma) include (high-K) calc-alkaline andesites, rhyolites, and minor shoshonitic (Chu et al., 2006; Hou et al., 2006; Mo et al., 2005, 2007; Zhu et al., 2011). Miocene magmatism in the Lhasa terrane is characterized by small volumes of (ultra) potassic lavas and adakite-like intrusions (Chung et al., 2003; Gao et al., 2007; Hou et al., 2013, 2015; Zheng et al., 2014; Yang et al., 2015, 2016).

Magmatic Cu-Mo, Pb-Zn-(Ag), Fe-Cu, and W-Mo deposits have been recognized in the Lhasa terrane, which constitute the Gangdese porphyry Cu-Mo belt in the southern Lhasa subterrane and the northern Gangdese Pb-Zn-Ag-Fe-Cu-Mo-W polymetallic belt (NGPB) in the central Lhasa subterrane (Hou et al., 2006, 2015; Hou and Cook, 2009; Yang et al., 2015, 2016; Zheng et al., 2015; Fu et al., 2017; Xu et al., 2017, 2021b). The NGPB extends for ~600 km along the Luobadui-Milashan Fault. Mineralization in the NGPB occurred during the main collisional stage (65–41 Ma) (Meng et al., 2007; Huang et al., 2012; Zhao et al., 2014; Zheng et al., 2015; Fu et al., 2017). Several ore-deposit types have been identified in this belt, including porphyry/skarn W-Mo, skarn Fe-(Cu), granite-related Pb-Zn-(Ag), and skarn polymetallic deposits (Fig. 1b) (Zheng et al., 2015; Fu et al., 2017). Porphyry/skarn W-Mo deposits occur in the easternmost margin of the central Lhasa subterrane and include the Hahaigang skarn W-Mo (63.2 Ma, Li et al., 2014), and Tangbula porphyry Mo-Cu (20.9 Ma, Wang et al., 2010) deposits. The skarn Fe-(Cu) deposits (65–49 Ma) are commonly associated with syn-collisional metaluminous granodiorites, monzogranites (Zheng et al., 2015 ; Zhang et al., 2019). The granite-related Pb-Zn-(Ag) deposits (65–55 Ma) are associated with peraluminous granite, quartz porphyry, and granite porphyry (Zheng et al., 2015). The granite-related Pb-Zn-(Ag) deposits include skarn-hosted, breccia-hosted, and porphyry-hosted deposits (Gao et al., 2011; Huang et al., 2012; Ji, 2013; Zheng et al., 2015; Fu et al., 2017; Zhang et al., 2019). The polymetallic skarn-type deposits are distributed in the eastern of the central Lhasa subterrane, including the Bangpu porphyry-skarn Mo-(Cu)-Pb-Zn deposit (15 Ma, Zhao et al., 2015), the Longmala skarn Fe-(Cu)-Pb-Zn deposit (56 Ma, Fu et al., 2014), and the Lietinggang-Leqingla skarn Pb-Zn-Fe-Cu-(Mo) deposit (58–59 Ma, Ma et al., 2020).

3. Geology of the Lietinggang-Leqingla deposit

The Lietinggang-Leqingla deposit is the largest skarn-type polymetallic deposit in the NGPB. It is situated in the northern Linzhou County of the central Lhasa subterrane (Fig. 1b). The volcanic-sedimentary rocks in the mining area belong to the Middle Permian Luobadui Formation, the Upper Permian Mengla Formation, the Upper Triassic Jialapu Formation, and the Eocene Nianbo Formation. The Luobadui Formation occurs in the southern part of the mining area and is dominated by (from south to north) andesitic basalt, medium-thick limestone and tuffaceous sandstone. The Mengla Formation crops out in the northern and southern part of the mining area and comprises tuffaceous sandstone, limestone interbedded with slate, and calcareous mudstone with intercalations siltstone. The Jialapu Formation (exposed in the centre of mining area) comprises sandstone, siltstone and mudstone, and are unconformably overlying the Permian strata. The Nianbo Formation occurs in the northwest of the mining area and is dominated by rhyolitic fused tuff with intercalations of volcanic breccia and tuffaceous conglomerate (Fig. 2). Within the southern part of the mining area, a near vertical normal fault with an east to west trend impacted the ore body, which is hosted in limestone interbedded with slate of the Mengla Formation. In the northern part of mining area a near-vertical north–south trending reverse fault has displaced the skarn in some areas.

3.1. Magmatism

The Jubuzhari felsic intrusions that are associated with mineralization are widely distributed in the Lietinggang-Leqingla deposit. It comprises three stocks and crops out over ~5 km^2 in the southeast of the mining area (Fig. 2). The felsic intrusions show a gradual granodiorite-granodiorite porphyry-granite porphyry transition from the center to the edge. Laser-ablation ICP-MS zircon U-Pb dating of the granodiorite, granodiorite porphyry, and granite porphyry yield similar crystallization ages of 62.4 ± 1.2 Ma, 62.6 ± 0.6 Ma, and 63.7 ± 1.0 Ma, respectively (Ma et al., 2015; Zhang et al., 2019). The quartz diorite occurs in the northern part of the mining area in the form of stock (Fig. 2). It shows a semi-automorphic granular in texture comprising plagioclase (~50%), K-feldspar (~10%), quartz (~15%), and hornblende and biotite (~20%), with accessory apatite, zircon and magnetite

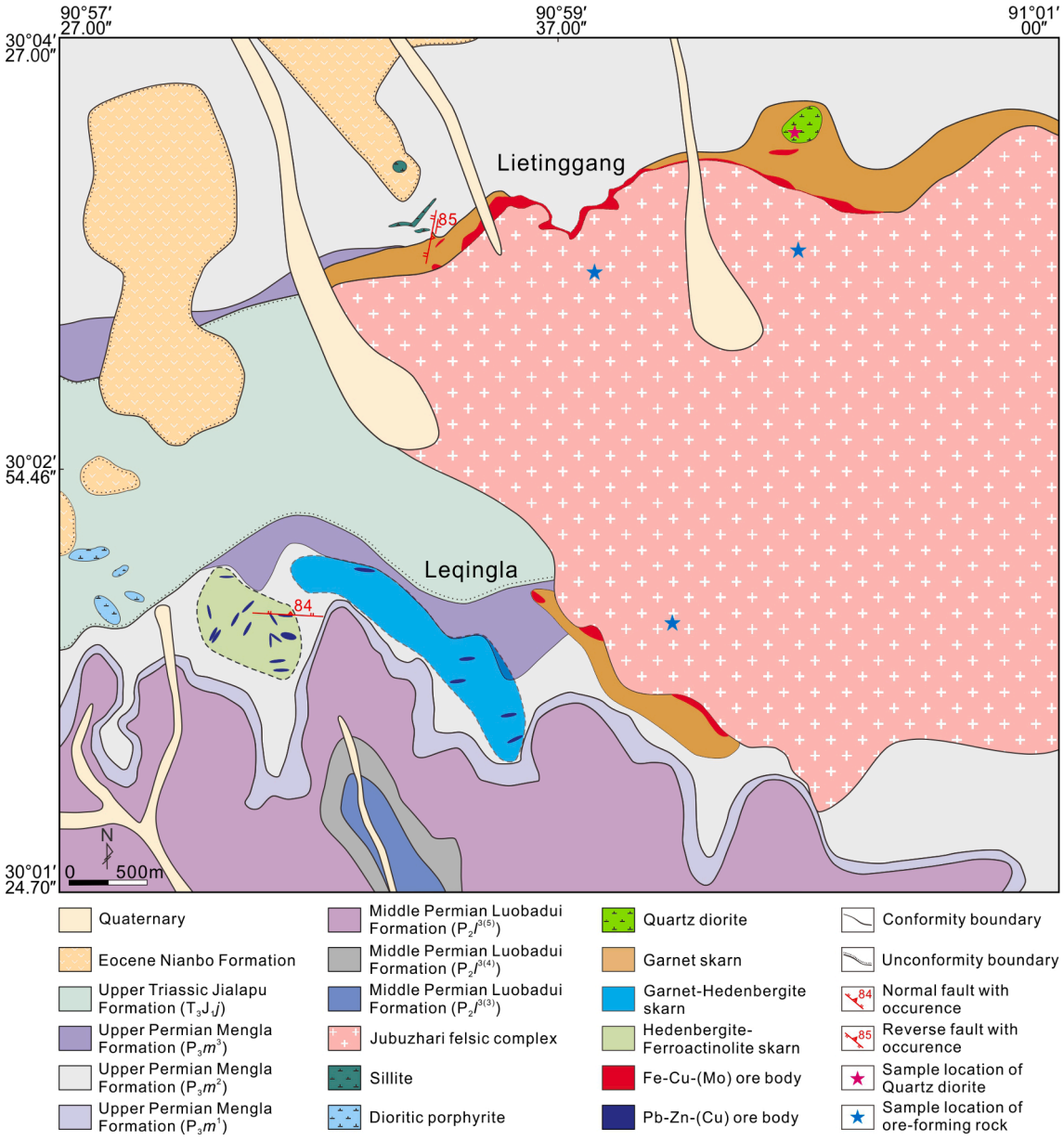

Fig. 2. Geological map of the Lietinggang-Leqingla Pb-Zn-Fe-Cu-(Mo) deposit.

(Fig. 3). Small-scale sillite and dioritic porphyrite stocks intruded into the limestone of the Mengla Formation and siltstone of the Jialapu Formation, respectively.

3.2. Orebodies of the Lietinggang-Leqingla deposit

The Lietinggang-Leqingla deposit includes the Lietinggang Fe-Cu-(Mo) ore bodies in the north and the Leqingla Pb-Zn-Fe-(Cu) ore bodies in the south. The Lietinggang Fe-Cu-(Mo) ore bodies are developed as stratiform, cystic or lenticular units in east–west trending garnet skarns along the contact of the Jubuzhari intrusions and the carbonate strata of the Mengla Formation (Fig. 2).

The Leqingla Fe-(Cu) ore bodies occurs as laminated, lenticular or irregular-shaped units and are situated in north–south trending garnet skarns along the contact between the Jubuzhari intrusions and carbonate strata of the Mengla Formation (Fig. 2). The Leqingla Pb-Zn-(Cu) ore bodies are hosted in garnet-pyroxene and pyroxene-actinolite skarns, which are more distal from the Jubuzhari intrusions compared to the Leqingla Fe-Cu ore bodies.

3.3. Alteration and mineralization

The mining area is characterized by a regular spatially zoned alteration and mineralization. Garnet skarns hosting Fe-Cu-Mo mineralization comprise garnet, diopside, hedenbergite, actinolite, epidote, and chlorite (Fig. 4d). The Fe-Cu-(Mo) mineralization is characterized by disseminated, massive, and vein-type occurrence of magnetite, chalcopyrite, and minor molybdenite (Fig. 4a). Chalcopyrite, pyrite, pyrrhotite with minor molybdenite, sphalerite and galena replaced the eu- and subhedral magnetite and early skarn minerals (Fig. 4b, g).

The garnet-pyroxene skarns and pyroxene-actinolite skarns hosting the Pb-Zn-(Cu) mineralization comprise hedenbergite, ferroactinolite, epidote, and minor garnet, chlorite, and sericite (Fig. 4e, f). The mineralization is characterized by the massive, disseminated, and vein-type occurrence of sphalerite, galena, chalcopyrite, pyrite, and pyrrhotite (Fig. 4c). Chalcopyrite is exsolved as an emulsion from the reddish-brown sphalerite or symbiotic with sphalerite and galena in an allotriomorphic granular form (Fig. 4h, i).

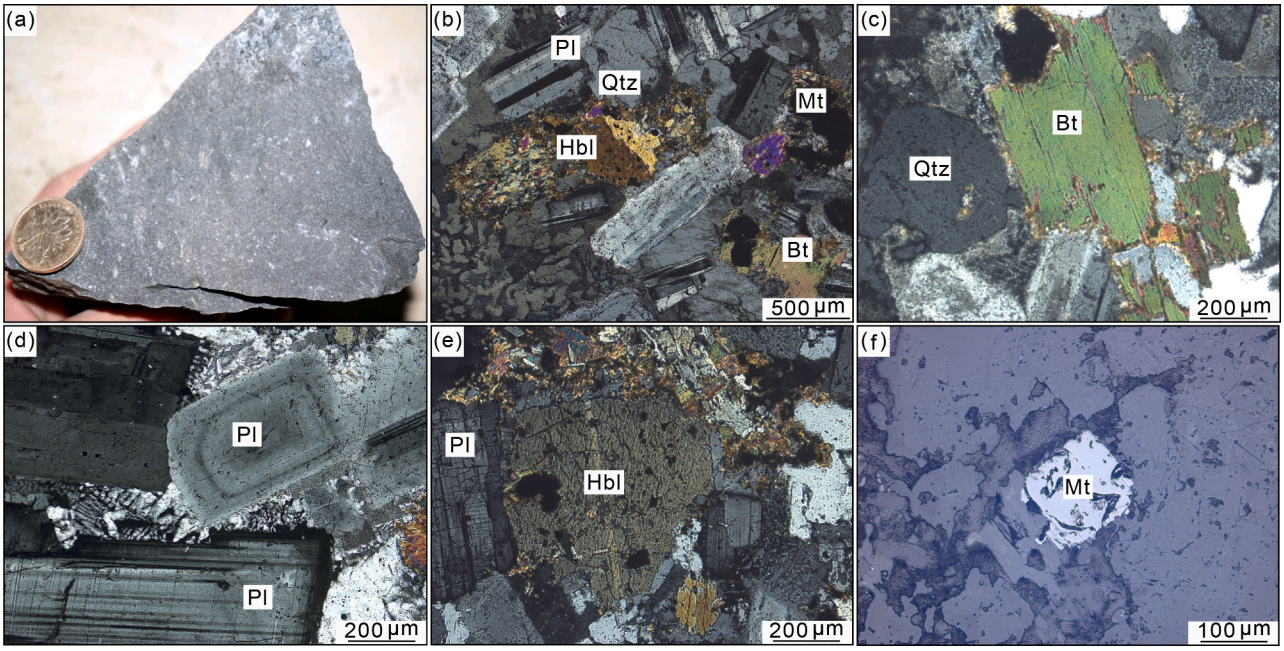

Fig. 3. Photomicrographs showing characteristics of the quartz diorite in the Lietinggang-Leqingla deposit. (a) Sample of the quartz diorite. (b) Mineral assemblage of quartz diorite with hornblende, biotite, plagioclase, quartz, and magnetite (crossed-polarized light). (c) Mineral assemblages of quartz diorite with quartz and biotite (crossed-polarized light). (d) Plagioclase in quartz diorite (crossed-polarized light). (e) Plagioclase and hornblende in quartz diorite (crossed-polarized light). (f) Magnetite in quartz diorite (reflected light). Hbl: hornblende, Bt: biotite, Pl: plagioclase, Qtz: quartz, Mt: magnetite.

4. Analytical methods

4.1. Zircon U-Pb age dating and trace elements

Laser ablation ICP-MS zircon U-Pb dating was done at the Mineral and Fluid Inclusion Microanalysis Lab (Institute of Geology, Chinese Academy of Geological Sciences, Beijing) using a NWR 193UC laser ablation system (Elemental Scientific Lasers, USA) equipped with Coherent 200 excimer laser and a Two Volume 2 ablation cell. The ablation system was coupled to an Agilent 7900 ICP-MS (Agilent, USA).

The zircon crystals were mounted in epoxy discs, polished to expose the grains, cleaned ultrasonically in ultrapure water, and then cleaned again prior to the analysis using AR grade methanol. The analysis was done using a 30 μm spot size with a 5 Hz and 2 J/cm^2 laser fluence.

Zircon 91500 was used as primary reference material and GJ-1 and the Plešovice were used as secondary reference materials. The 91500 was analyzed twice and both of GJ-1 and Plešovice were analyzed once every 10–12 analyses. Typically, 35–40 s of the sample signals were acquired after a 20 s of gas background measurement. NIST610 and 91Zr were used as external and internal standard, respectively, for trace element analysis. The measured ages of the reference materials used are as follows: 91500 (1061.5 ± 3.2 Ma, 2σ), GJ-1 (604 ± 6 Ma, 2σ), and Plešovice (340 ± 4 Ma, 2σ), which agreed well with the nominal values within the defined uncertainty. The Iolite software package was used for data reduction (Paton et al., 2010).

4.2. Zircon Lu-Hf isotope geochemistry

In-situ Lu-Hf isotope measurements were done using a Thermo Finnigan Neptune-plus MC-ICP-MS fitted with a J-100 femto-second laser ablation system Applied Spectra Inc. at the National Research Center for Geoanalysis, Chinese Academy of Geological Sciences. The analytical procedures and calibration methods are similar to those described by Wu et al. (2006). Zircons were ablated for 31 s at a repetition rate of 8 Hz at 1.5 J/cm^2. The ablation pits were 20 × 40 μm in diameter. During the analysis, the isobaric interference of ^{176}Lu on ^{176}Hf was negligible due to extremely low ^{176}Lu/^{177}Hf values in zircon (normally < 0.002). The mean ^{173}Yb/^{172}Yb value of individual spots was used to calculate the fractionation coefficient (β_{Yb}) and then to calculate the contribution of ^{176}Yb to ^{176}Hf. An isotopic ^{173}Yb/^{172}Yb ratio of 1.35274 was used.

4.3. Whole rock major and trace element geochemistry

All samples for geochemical analyses were ground to ~200 mesh sizes using an agate mortar. Major, and trace, and rare earth elements were measured using X-ray fluorescence spectrometry (XRF) and inductively coupled plasma mass spectrometry (ICP-MS) respectively at the National Research Centre of Geoanalysis, Chinese Academy of Geological Science. The analytical uncertainty of XRF analyses for major elements was <2% relative. The standards GSR1 and GSD9 were used to monitor data quality during the analysis. The 2σ uncertainties based on repeated measurements of these standards are <10% for elements with abundances <10 ppm and <5% for elements with abundances >10 ppm.

4.4. Whole rock Sr-Nd isotope geochemistry

Whole-rock Sr-Nd isotopic analyses were measured on a Finnigan MAT 262 mass-spectrometer at the Key Laboratory of Crust-Mantle Materials and Environments (University of Science and Technology of China). The method of chemical separation of Rb, Sr, Sm, Nd, and detailed analytical procedures are described by Chen et al. (2007). ^{87}Sr/^{86}Sr and ^{143}Nd/^{144}Nd ratios were normalized to ^{86}Sr/^{88}Sr = 0.1194 and ^{146}Nd/^{144}Nd = 0.7219, respectively. Repeated measurements of the Ames metal and the NBS987 Sr standard gave mean values of 0.512143 ± 0.000015 (n = 6) for the ^{143}Nd/^{144}Nd ratio and 0.710246 ± 0.000018 (n = 5) for the ^{87}Sr/^{86}Sr ratio (2σ error). Total procedural blanks were <300 pg for Sr and <50 pg for Nd (Chen et al., 2009).

5. Analytical results

5.1. Zircon U-Pb geochronology

Eu- to subhedral zircon grains in quartz diorite are transparent, colorless, and show oscillatory growth zoning (Fig. 5a). They are

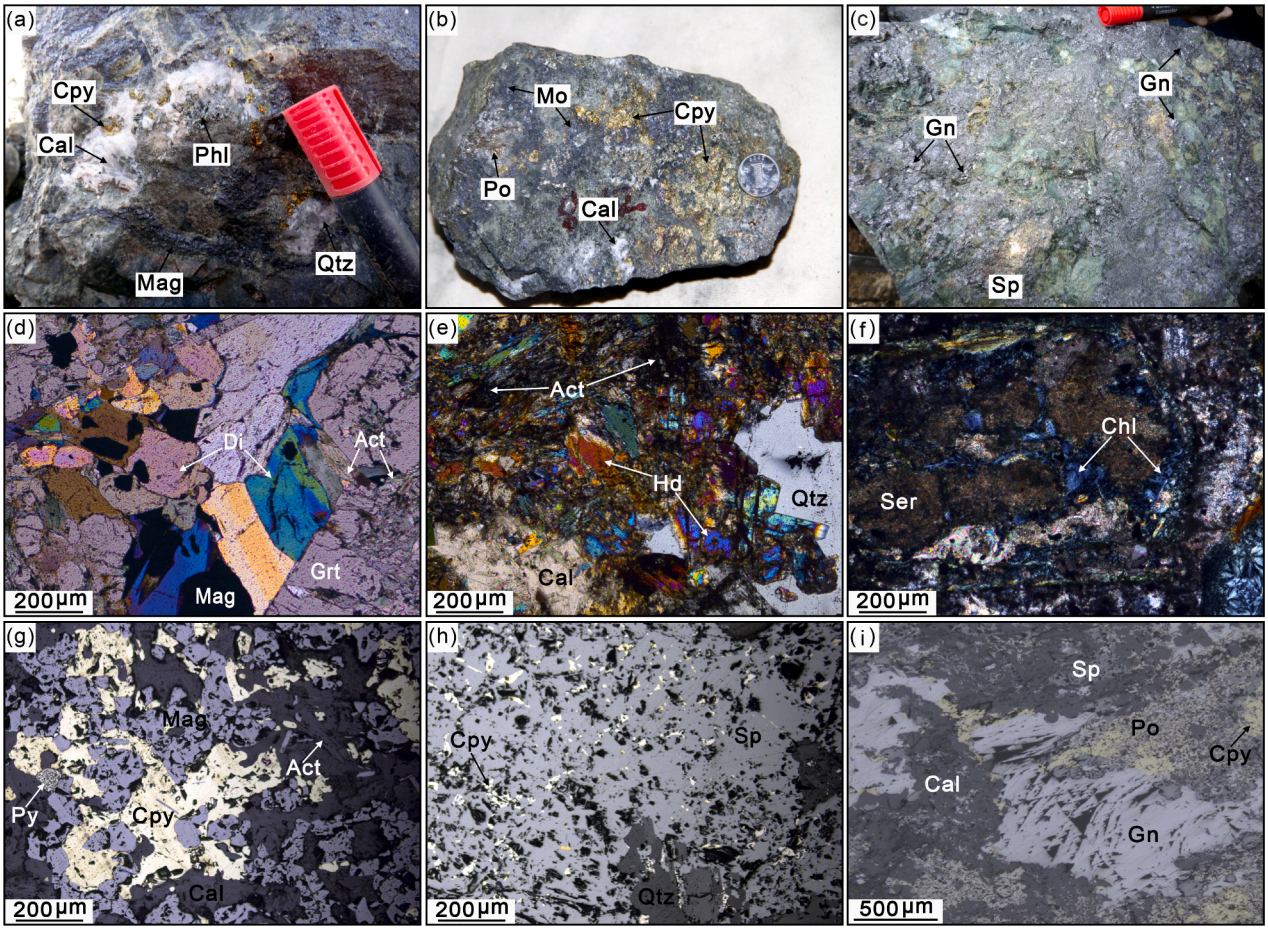

Fig. 4. Hand specimen photographs and photomicrographs showing the alteration and mineralization in the Lietinggang-Leqingla deposit. (a) Banded magnetite, disseminated chalcopyrite, calcite, quartz, and phlogopite in skarn from the Fe-Cu-(Mo) ore deposit. (b) Disseminated chalcopyrite, molybdenite, and pyrrhotite from the Fe-Cu-(Mo) ore deposit; (c) Disseminated sphalerite, and galena in skarn from the Pb-Zn-Cu ore deposit. (d) Subhedral magnetite and radial actinolite metasomatic early garnet and diopside from the Fe-Cu-(Mo) ore deposit (crossed-polarized light). (e) Quartz-calcite alteration of early garnet, and hedenbergite from the Pb-Zn-Cu ore deposit (crossed-polarized light). (f) Skarn mineral assemblages of chlorite and sericite (crossed-polarized light). (g) Pyrite-chalcopyrite alteration of early magnetite, and actinolite from the Fe-Cu-Mo ore deposit (reflected light). (h) Chalcopyrite is exsolved as emulsion in the massive sphalerite and quartz from the Pb-Zn-Cu ore deposit (reflected light). (i) Galena, sphalerite, chalcopyrite, pyrrhotite, and calcite from the Pb-Zn-Cu ore deposit (reflected light). Grt: garnet, Di: diopside, Hd: hedenbergite, Act: actinolite, Ep: epidote, Chl: chlorite, Phl: phlogopite, Ser: sericite, Cal: calcite, Qtz: quartz, Mag: magnesite, Cpy: chalcopyrite, Mo: molybdenite, Py: pyrite, Po: pyrrhotite, Sp: sphalerite, Gn: galena.

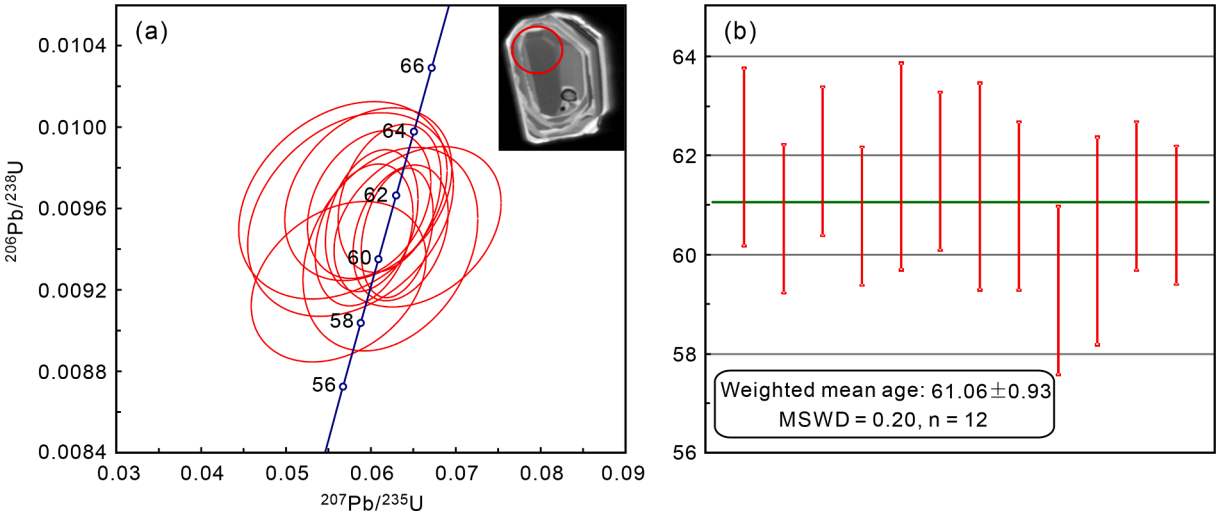

Fig. 5. Zircon U-Pb concordia diagrams (a) and weighted mean age diagrams (b) of quartz diorite in the Lietinggang-Leqingla deposit.

80–150 μm in length with elongation ratios of 1.5:1 to 3:1. The results of LA-ICP-MS zircon U-Pb analysis are listed in Table 1. The quartz diorite yields a weighted mean U-Pb zircon age of 61.06 ± 0.93 Ma (1σ, MSWD = 0.20, n = 12), which represents the crystallization age of the quartz diorite (Fig. 5b). Zircon U-Pb ages have been reported for the granodiorite (62.4 ± 1.2 Ma), granite porphyry (63.6 ± 1.0 Ma), and granodiorite porphyry of 62.6 ± 0.6 Ma (Zhang et al., 2019). The overlapping ages indicate that the quartz diorite and the Jubuzhari felsic intrusions are coeval.

5.2. Whole-rock major and trace element geochemistry

The whole-rock major and trace element results of Lietinggang-Leqingla quartz diorite are shown in Table 2. The five samples are characterized by low SiO_2 (61.57–65.88) and high total alkali contents ($Na_2O + K_2O$ = 5.69–6.35), plotting in the subalkaline or tholeiite series fields (Fig. 6a). They have a consistent K_2O content (2.53–3.07), and show a High-K calc-alkaline affinity (Fig. 6b). In the chondrite-normalized REE diagram (Fig. 7a), the quartz diorites display LREE enrichment relative to HREE, with $(La/Yb)_N$ and LREE/HREE mass ratios of 4.29–7.07 (average value of 6.36) and 4.80–7.10 (average value of 6.49), respectively, and a moderately negative Eu anomalies (Eu/Eu* = 0.49–0.72). Primitive mantle-normalized incompatible element patterns show significant large ion lithophile elements (LILE) enrichment (e.g., Rb, Th, U, and Ba) and high field strength elements depletion (e.g., Nb, Ta, Sr, P, and Ti) (Fig. 7b). Furthermore, all the samples exhibit arc volcanic geochemical characteristics, i.e., high Y (25.4–28.5 ppm) and low Sr (255–369 ppm) contents, and low Sr/Y mass ratios (9–15). The geochemical signatures of quartz diorite are similar to those of the granitoid and diorite in the Lietinggang-Leqingla deposit (Figs. 6c, 7b).

5.3. Zircon Hf isotopes

Lu-Hf isotopic analyses of zircons from the quartz diorite (Table 3) were performed on the same grains as for the U-Pb ages. The zircon grains yield $^{176}Hf/^{177}Hf$ isotopic ratios of 0.282739–0.282835, $^{176}Lu/^{177}Hf$ isotopic ratios of 0.000942–0.003310, and ε_{Hf} (t) values of 0.14–3.46, with T^C_{DM} model ages ranging from 911 to 1124 Ma.

5.4. Whole rock Sr-Nd isotopes

Whole-rock Sr-Nd isotopic compositions of the quartz diorite are given in Table 4. Initial Sr isotopic ratios ($^{87}Sr/^{86}Sr)_i$ and Nd values [ε_{Nd} (t)] are calculated for the weighted mean age of 61.06 Ma. The samples exhibit a small range in initial $^{87}Sr/^{86}Sr$ (0.706355–0.706807) and ε_{Nd} (t) values of −2.08 to −1.57, with T_{DM2} model ages of 996–1038 Ma.

Table 2
Whole-rock major (wt.%) and trace element (ppm) data of the quartz diorite from the Lietinggang-Leqingla deposit.

Sample	LTG15-4–2	LTG15-4–3	LTG15-4–4	LTG15-4–5	LTG15-4–6
Rock-type	Quartz diorite	Quartz diorite	Quartz diorite	Quartz diorite	Quartz diorite
SiO_2	65.88	62.11	61.69	61.88	61.57
TiO_2	0.63	0.75	0.73	0.75	0.76
Al_2O_3	14.50	15.53	14.97	15.42	15.47
TFe_2O_3	5.72	7.33	7.64	8.59	7.69
MnO	0.11	0.11	0.06	0.09	0.10
MgO	1.87	2.54	2.64	2.68	2.57
CaO	4.26	5.19	5.11	5.23	5.23
Na_2O	3.28	3.12	3.11	3.21	3.16
K_2O	3.07	2.72	2.65	2.62	2.53
P_2O_5	0.12	0.16	0.16	0.16	0.17
LOI	0.52	0.45	0.45	0.16	0.37
Total	99.96	100.01	99.21	100.79	99.62
A/CNK	1.37	1.41	1.38	1.39	1.42
V	99.9	137.0	141.0	142.0	138.0
Cr	68.3	105.0	87.1	193.0	154.0
Co	11.1	17	15.1	16.4	17.4
Ni	14.5	19.7	17.5	28.9	25.0
Rb	100	102	102	92	95.9
Sr	255	333	369	357	332
Y	28.0	25.6	25.4	28.4	28.5
Zr	199	182	171	174	194
Nb	7.40	7.08	6.82	7.02	6.98
Cs	4.29	5.20	5.26	4.81	5.29
Ba	427	396	392	430	396
La	29.7	27.7	15.5	25.7	27.2
Ce	63.1	58.2	31.3	54.0	56.6
Pr	7.98	7.4	4.19	6.79	7.14
Nd	30.9	28.7	17.7	26.1	27.3
Sm	5.60	5.23	3.64	4.82	4.93
Eu	0.87	0.99	0.88	0.95	0.98
Gd	5.15	4.82	3.74	4.55	4.5
Tb	0.85	0.77	0.61	0.73	0.73
Dy	5.70	5.03	4.11	4.75	4.75
Ho	1.10	1.00	0.84	0.94	0.95
Er	3.43	3.05	2.59	2.87	2.95
Tm	0.48	0.44	0.37	0.4	0.42
Yb	3.20	2.91	2.59	2.65	2.76
Lu	0.48	0.44	0.39	0.41	0.42
Hf	5.67	5.07	4.79	4.76	5.21
Ta	0.65	0.59	0.54	0.54	0.56
Pb	14.2	14.7	11.8	12.1	14.9
Th	12.8	8.8	7.43	8.24	7.89
U	3.11	1.79	1.71	2.05	1.81
Sr/Y	9.11	13.01	14.53	12.57	11.65
$(La/Yb)_N$	6.66	6.83	4.29	6.96	7.07
Eu/Eu*	0.49	0.59	0.72	0.61	0.62

LOI = loss of ignition, A/CNK = $Al_2O_3/(CaO + Na_2O + K_2O)$ (molar ratio), Eu/Eu* = $2 \times Eu_N / (Sm_N + Gd_N)$.

Table 1
Zircon LA-ICP-MS U-Pb isotopic data from the quartz diorite in Lietinggang-Leqingla deposit.

Spot	Pb	Th	U	Th/U	$^{207}Pb/^{206}Pb$		$^{207}Pb/^{235}U$		$^{206}Pb/^{238}U$		$^{207}Pb/^{206}Pb$		$^{207}Pb/^{235}U$		$^{206}Pb/^{238}U$	
	ppm	ppm	ppm		Ratio	± 1σ	Ratio	± 1σ	Ratio	± 1σ	Age	± 1σ	Age	± 1σ	Age	± 1σ
LTG15-4-1	8.43	296.2	257.3	1.16	0.0448	0.0046	0.0597	0.0065	0.00967	0.00028	−120.0	190.0	59.0	6.3	62.0	1.8
LTG15-4-2	13.05	474.0	788.0	0.60	0.0453	0.0028	0.0592	0.0038	0.00947	0.00023	−70.0	110.0	58.1	3.6	60.7	1.5
LTG15-4-3	11.10	397.2	507.6	0.79	0.0474	0.0031	0.0622	0.0040	0.00965	0.00024	10.0	120.0	61.5	3.9	61.9	1.5
LTG15-4-4	15.30	550.0	854.0	0.65	0.0482	0.0027	0.0635	0.0037	0.00948	0.00022	90.0	110.0	62.3	3.6	60.8	1.4
LTG15-4-5	5.33	199.6	199.6	1.00	0.0437	0.0065	0.0567	0.0081	0.00964	0.00032	−340.0	220.0	54.8	7.7	61.8	2.1
LTG15-4-6	11.15	392.6	505.1	0.78	0.0452	0.0036	0.0598	0.0048	0.00962	0.00024	−90.0	140.0	58.6	4.5	61.7	1.6
LTG15-4-7	4.20	155.3	161.8	0.96	0.0446	0.0063	0.0576	0.0080	0.00957	0.00033	−270.0	230.0	56.5	7.7	61.4	2.1
LTG15-4-8	4.95	171.5	287.1	0.60	0.0494	0.0048	0.0655	0.0065	0.00951	0.00026	30.0	180.0	63.7	6.2	61.0	1.7
LTG15-4-9	4.57	162.3	280.2	0.56	0.0443	0.0054	0.0562	0.0068	0.00924	0.00026	−230.0	200.0	54.8	6.5	59.3	1.7
LTG15-4-10	12.71	465.9	461.0	1.02	0.0485	0.0056	0.0623	0.0068	0.0094	0.00033	80.0	230.0	61.1	6.5	60.3	2.1
LTG15-4-11	17.74	674.0	763.0	0.88	0.0457	0.0027	0.0601	0.0036	0.00954	0.00023	−40.0	110.0	59.1	3.4	61.2	1.5
LTG15-4-12	69.00	2475.0	1418.0	1.75	0.0480	0.0019	0.0631	0.0028	0.00948	0.00021	81.0	83.0	62.0	2.6	60.8	1.4

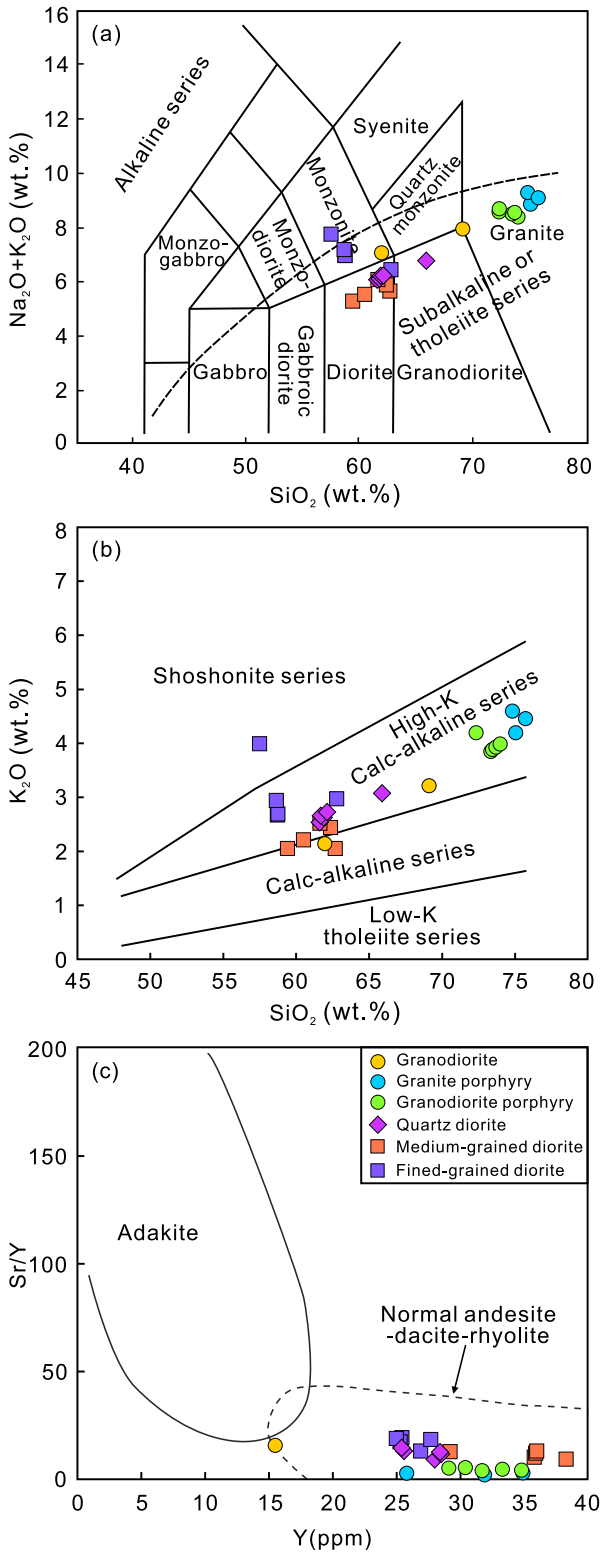

Fig. 6. Classification diagram of the ore-forming suites from Lietinggang-Leqingla deposit, including (a) ($Na_2O + K_2O$) vs. SiO_2 (Rollinson, 1993), (b) K_2O vs. SiO_2 (Rickwood, 1989), and (c) Y vs. Sr/Y (Drummond and Defant, 1990). Data of the granodiorite, granite porphyry, and granodiorite porphyry are from Zhang et al. (2019), data of the medium- and fine-grained diorite are from Wang et al. (2018).

5.5. Zircon trace elements

The zircon trace element compositions from the samples are listed in Table 5, and all zircon grains display positively sloped chondrite-normalized REE patterns (Fig. 8a). They are characterized by depleted in LREE and enriched in HREE, with a moderately negative Eu anomalies and positive Ce anomalies. Eu and Ce are sensitive to magmatic oxidation state due to they occur in two valence states in magmas (Eu^{2+} and Eu^{3+}, and Ce^{3+} and Ce^{4+}) (Ballard et al., 2002; Burnham et al., 2015). Thus, zircon Eu anomaly (Eu/Eu*) and Ce anomaly (Ce/Ce*, Ce^{4+}/Ce^{3+}) can be used to reflect the oxygen fugacity of the magma (Dilles et al., 2015; Loader et al., 2017). The zircon Eu/Eu* ($Eu_N/[Sm_N \times Gd_N]^{1/2}$) from the quartz diorite are 0.03 to 0.21 (with an average of 0.11), which is lower than those of granodiorite, granodiorite porphyry, and granite porphyry (Fig. 8b). The Ce anomalyare calculated by the formula $Ce/Ce^* = Ce_N/([Nd_N]^2/Sm_N)$ proposed by Loader et al. (2017). The results show that zircon from the quartz diorite have Ce/Ce* ratios between 9.39 and 96.13. In addition, zircon Ce^{3+}/Ce^{4+} ratios are generally considered as another proxy for the zircon Ce anomaly (Ballard et al., 2002; Qiu et al., 2013), and our results show that the quartz diorite hasCe^{3+}/Ce^{4+} ratios of 12.92 to 158.78. In general, these are similar to the granodiorite, granodiorite porphyry, and granite porphyry (Fig. 8c).

The crystallization temperature of zircon can be estimates using the Ti-in-zircon thermometer (Watson et al., 2006; Ferry and Watson, 2007). Zircons in the quartz diorite have crystallization temperature of 718° to 794 °C, with an average of 768 °C, which is higher than those of granodiorite, granodiorite porphyry, and granite porphyry (Fig. 8d). The zircon Dy/Yb and (Ce/Nd)/Y ratios have been proposed as a proxy for the magmatic water content, and magma with high water content is character by Dy/Yb < 0.3, and (Ce/Nd)/Y > 0.01 (Lu et al., 2016). The results show that Dy/Yb ratios of zircon grains from quartz diorite are ranging from 0.25 to 0.41 with an average of 0.33, which is higher than that of the granodiorite, granodiorite porphyry, and granite porphyry (Fig. 8d).

6. Discussion

6.1. Geochronology

The intermediate-acid intrusions associated with mineralization in the mining area mainly include granodiorite, granite porphyry, granodiorite porphyry, medium- and fine-grained diorite, with zircon U-Pb ages of 62.4 ± 1.2 Ma, 63.7 ± 1.0 Ma, 62.6 ± 0.6 M a, 61.9 ± 0.5 M a, and 62.0 ± 0.6 M a, respectively (Wang et al., 2018; Zhang et al., 2019). The zircon U-Pb dating of quartz diorite, which is associated with mineralization and emplaced as stock in the northeast of the mine area (Fig. 2), yield a consistent age of 61.06 ± 0.63 Ma. The molybdenite Re-Os and sphalerite Rb-Sr isochron ages indicate that the mineralization at the Lietinggang-Leqingla Pb-Zn-Fe-Cu-(Mo) deposit occurred at 59–58 Ma (Ma et al., 2020). The similarity between the zircon U-Pb ages of the ore-forming intrusions and the molybdenite Re-Os and sphalerite Rb-Sr isochron ages suggest a close relationship between the Pb-Zn-Fe-Cu-(Mo) mineralization and the intrusions. These ages also indicate that the igneous activity and related skarn Pb-Zn-Fe-Cu-(Mo) mineralization occurred during the main stage of the Indian-Asian continental collision (Hou et al., 2006; Hou and Cook, 2009), which is consistent with most deposits found in the northern Gangdese Pb-Zn-Ag-Fe-Cu-Mo-W polymetallic belt, i.e., the Narusongduo Pb-Zn, the Jiaduopule Fe-Cu, and the Hahaigang W-Mo deposits (Yu et al., 2011; Ji et al., 2012; Li et al., 2014).

6.2. Petrogenesis of the ore-forming intrusions

6.2.1. Genetic type and magma source

The ore-forming intrusions from the Lietinggang-Leqingla deposit, i.e., granodiorite, granite porphyry, granodiorite porphyry, quartz

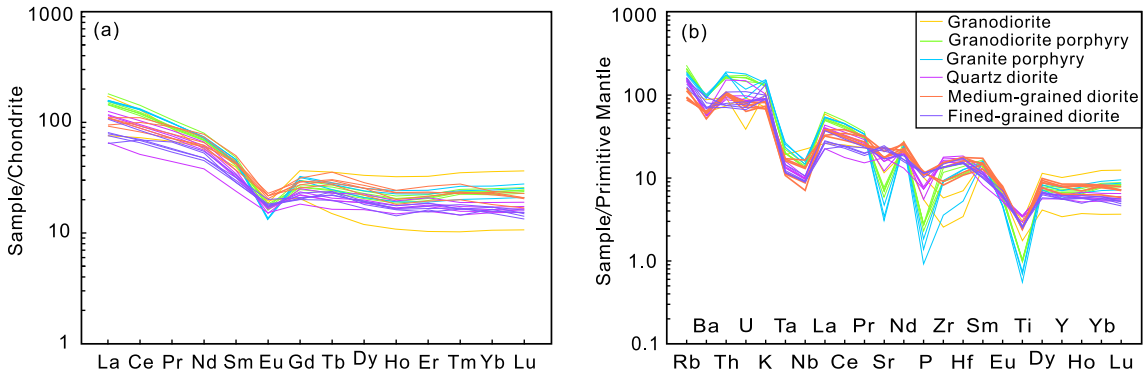

Fig. 7. (a) Chondrite-normalized REE patterns and (b) primitive-mantle-normalized trace element diagrams for the ore-forming suites from Lietinggang-Leqingla deposit. The chondrite and primitive mantle values are from Sun and McDonough, 1989. Data sources are the same as in Fig. 6.

Table 3
Hf isotopic data of zircons from the quartz diorite in Lietinggang-Leqingla deposit.

Sample	Age	$^{176}Hf/^{177}Hf$	2σ	$^{176}Lu/^{177}Hf$	2σ	$\varepsilon_{Hf}(t)$	T_{DM}/Ma	T^{C}_{DM}/Ma	$f_{Lu/Hf}$
LTG15-4-1-1	62.0	0.282821	0.000024	0.003310	0.000029	2.97	650.15	943.71	−0.90
LTG15-4-1-2	60.7	0.282835	0.000020	0.002148	0.000019	3.46	609.89	911.23	−0.94
LTG15-4-1-3	61.9	0.282801	0.000016	0.001549	0.000024	2.34	647.69	984.12	−0.95
LTG15-4-1-4	60.8	0.282830	0.000017	0.001469	0.000010	3.33	605.02	919.46	−0.96
LTG15-4-1-5	61.8	0.282739	0.000018	0.000942	0.000012	0.14	725.76	1124.30	−0.97
LTG15-4-1-6	61.7	0.282823	0.000015	0.001297	0.000021	3.11	612.29	934.44	−0.96
LTG15-4-1-7	61.4	0.282800	0.000023	0.001298	0.000022	2.28	645.62	987.41	−0.96
LTG15-4-1-8	61.0	0.282769	0.000019	0.001887	0.000037	1.16	700.26	1058.17	−0.94
LTG15-4-1-9	59.3	0.282804	0.000016	0.001357	0.000007	2.39	640.36	978.86	−0.96
LTG15-4-1-10	60.3	0.282769	0.000017	0.001548	0.000009	1.17	693.49	1057.20	−0.95
LTG15-4-1-11	61.2	0.282825	0.000019	0.001114	0.000038	3.18	606.36	929.60	−0.97
LTG15-4-1-12	60.8	0.282771	0.000018	0.001791	0.000023	1.22	696.28	1054.69	−0.95

$T_{DM} = (1/\lambda) \times \ln(1 + (({}^{176}Hf/{}^{177}Hf)_s - ({}^{176}Hf/{}^{177}Hf)_{DM})/(({}^{176}Lu/{}^{177}Hf)_s - ({}^{176}Lu/{}^{177}Hf)_{DM})$, $T^{C}_{DM} = T_{DM} - (T_{DM} - t) \times (f_{cc} - f_s)/(f_{cc} - f_{DM})$. $\lambda = 1.867 \times 10^{-11} year^{-1}$; $({}^{176}Lu/{}^{177}Hf)_{DM} = 0.0384$. $({}^{176}Hf/{}^{177}Hf)_{DM} = 0.28325$ (Griffin et al., 2000), $f_{cc} = -0.5482$ (Griffin et al., 2002); $f_{DM} = 0.157$.

Table 4
Sr-Nd isotopic data of the quartz diorite in Lietinggang-Leqingla deposit.

Sample	Rock-type	$^{87}Rb/^{86}Sr$	$^{87}Sr/^{86}Sr$	$(\pm 2\sigma_m)$	$^{147}Sm/^{144}Nd$	$^{143}Nd/^{144}Nd$	$(\pm 2\sigma_m)$	$(^{87}Sr/^{86}Sr)_i$	$(^{143}Nd/^{144}Nd)_t$	$\varepsilon_{Nd}(t)$	T_{DM2}(Ma)
LTG15-4-2	Quartz diorite	1.135	0.707179	0.000013	0.1096	0.512511	0.000007	0.706807	0.512467	−1.80	1015
LTG15-4-3	Quartz diorite	0.886	0.706975	0.000013	0.1102	0.512497	0.000006	0.706685	0.512453	−2.08	1038
LTG15-4-4	Quartz diorite	0.800	0.706787	0.000010	0.1243	0.512521	0.000006	0.706525	0.512471	−1.72	1009
LTG15-4-5	Quartz diorite	0.746	0.706599	0.000014	0.1116	0.512524	0.000007	0.706355	0.512479	−1.57	996
LTG15-4-6	Quartz diorite	0.836	0.706962	0.000015	0.1092	0.512501	0.000007	0.706688	0.512458	−1.99	1030

$({}^{87}Sr/{}^{86}Sr)_i = ({}^{87}Sr/{}^{86}Sr)s - ({}^{87}Rb/{}^{86}Sr) \times (e^{\lambda T} - 1)$; $\lambda_{Rb\text{-}Sr} = 1.42 \times 10^{-11}$ $year^{-1}$, $^{87}Rb/^{86}Sr = (Rb/Sr) \times 2.8956$;
$\varepsilon_{Nd}(t) = [({}^{143}Nd/{}^{144}Nd)_i/({}^{143}Nd/{}^{144}Nd)_{CHUR}(t) - 1] \times 10{,}000$, $({}^{143}Nd/{}^{144}Nd)_i = ({}^{143}Nd/{}^{144}Nd)s - ({}^{147}Sm/{}^{144}Nd) \times (e^{\lambda T} - 1)$, $({}^{143}Nd/{}^{144}Nd)_{CHUR}(t) = 0.512638 - 0.1967 \times (e^{\lambda T} - 1)$, $\lambda_{Sm\text{-}Nd} = 6.54 \times 10^{-12}$ $year^{-1}$, $^{147}Sm/^{144}Nd = (Sm/Nd) \times 0.60456$ and t = 298 Ma;
$T_{DM} = 1/\lambda_{Sm\text{-}Nd} \times \ln\{1 + [(({}^{143}Nd/{}^{144}Nd)_S - 0.51315)/(({}^{147}Sm/{}^{144}Nd)_S - 0.21357)]\}$.

diorite, medium-grained diorite, and fine-grained diorite, have similar geochemical signatures. They are characterized by fractionated REE patterns with high LREE contents relative to HREE, LILE enrichment (e.g., Rb, Th, U, Ba), and a significantly depletion of high field strength elements including Nb, Ta, Sr, P, and Ti (Fig. 7). Furthermore, the ore-forming intrusions display similar zircon Hf isotopic compositions (Fig. 9a) and they exhibit negative correlations between the SiO_2 and CaO, Al_2O_3, MgO, FeO, P_2O_5, TiO_2 contents (Fig. 10). Collectively, these geochemical characteristics indicate that the ore-forming intrusions share a similar magma source and have a close genetic relationship.

Chappell and White (1992) proposed that S-type granites are generally peraluminous in nature and have a high $Al_2O_3/(CaO + Na_2O + K_2O)$ (A/CNK > 1.1) molar ratio whereas I-type granites are metaluminous to slightly peraluminous with A/CNK values of < 1.1. The metaluminous quartz diorite from the Lietinggang-Leqingla deposit shows an affinity with I-type granites as exemplified by relatively low A/CNK values (0.87–0.89) and a positive correlation between P_2O_5 and SiO_2 (Fig. 10e). In conclusion, the geochemical characteristics presented in this study and in previous studies (Wang et al., 2018; Zhang et al., 2019) indicate that the ore-forming intrusions in the Lietinggang-Leqingla deposit can be classified as I-type granites.

Four models have been proposed for the petrogenesis of the I-type granitoids: (1) assimilation and fractional crystallization of mantle derived parental basaltic magmas (Grove et al., 1997; Duchesne et al., 1998; Sisson et al., 2005); (2) partial melting of crustal materials (Chung et al., 2003); (3) mixing of felsic and mantle-derived basaltic magmas (Streck et al., 2007; Danyushevsky et al., 2008); (4) reworking of supra-crustal sedimentary materials by mantle-like magmas (Kemp et al., 2007).

Compared with the intermediate to felsic Paleocene intrusive-volcanic rocks, there are not many outcrops of the coeval mafic igneous rocks in this deposit. Furthermore, magmatism in the central

Table 5
Zircon trace elements data of quartz diorite in Lietinggang-Leqingla deposit.

Sample number	LTG15-4-1	LTG15-4-2	LTG15-4-3	LTG15-4-4	LTG15-4-5	LTG15-4-7	LTG15-4-8	LTG15-4-10	LTG15-4-15
Rock type	Quartz porphyry	Quartz porphyry	Quartz porphyry	Quartz porphyry	Quartz porphyry	Quartz porphyry	Quartz porphyry	Quartz porphyry	Quartz porphyry
La	0.06	1.05	0.08	0.13	0.03	0.02	0.62	0.07	0.02
Ce	18.69	38.40	27.85	40.70	12.27	12.79	12.36	11.58	29.40
Pr	0.48	0.18	0.12	0.19	0.38	0.29	0.32	0.28	0.34
Nd	6.99	2.55	2.02	2.45	5.30	5.28	1.86	4.49	4.78
Sm	11.90	5.93	4.78	5.67	9.72	9.51	3.42	6.61	9.41
Eu	2.07	0.23	0.34	0.12	1.22	0.92	0.34	0.57	0.46
Gd	77.30	36.70	27.20	35.10	50.20	45.90	20.50	35.60	55.70
Tb	27.43	13.28	10.05	12.17	16.47	14.30	7.66	10.83	19.86
Dy	336.10	173.10	122.20	160.80	192.10	169.60	101.20	133.10	251.00
Ho	127.80	69.70	47.00	61.20	70.40	60.20	38.80	49.50	93.30
Er	600.00	362.00	234.90	306.10	328.60	268.10	203.30	227.00	435.00
Tm	111.70	74.70	47.20	61.90	59.90	50.90	40.80	42.90	86.70
Yb	942.00	687.00	420.70	541.00	506.00	413.80	378.90	357.90	757.00
Lu	190.60	143.70	83.70	107.00	100.70	82.60	77.60	72.10	146.00
Ti	16.10	14.10	15.10	10.40	17.80	17.00	7.68	15.40	10.70
Ce^{4+}/Ce^{3+}	20.80	158.78	118.86	150.23	13.73	12.92	69.16	16.41	49.14
Eu/Eu*	0.21	0.05	0.10	0.03	0.18	0.14	0.12	0.11	0.06
Ce/Ce*	13.81	96.13	73.83	92.28	9.74	9.39	43.34	11.71	31.55
T (°C)	785	772	779	744	794	790	718	780	747
Dy/Yb	0.36	0.25	0.29	0.30	0.38	0.41	0.27	0.37	0.33

Notes: $Eu/Eu^* = Eu_N/[Sm_N \times Gd_N]^{1/2}$, $Ce/Ce^* = Ce_N/([Nd_N]^2/Sm_N)$ (Loader et al., 2017); Ce^{4+}/Ce^{3+} are calculated by the method from Ballard et al. (2002) and Qiu et al. (2013); T (°C) are calculated by the method from Ferry and Watson, 2007.

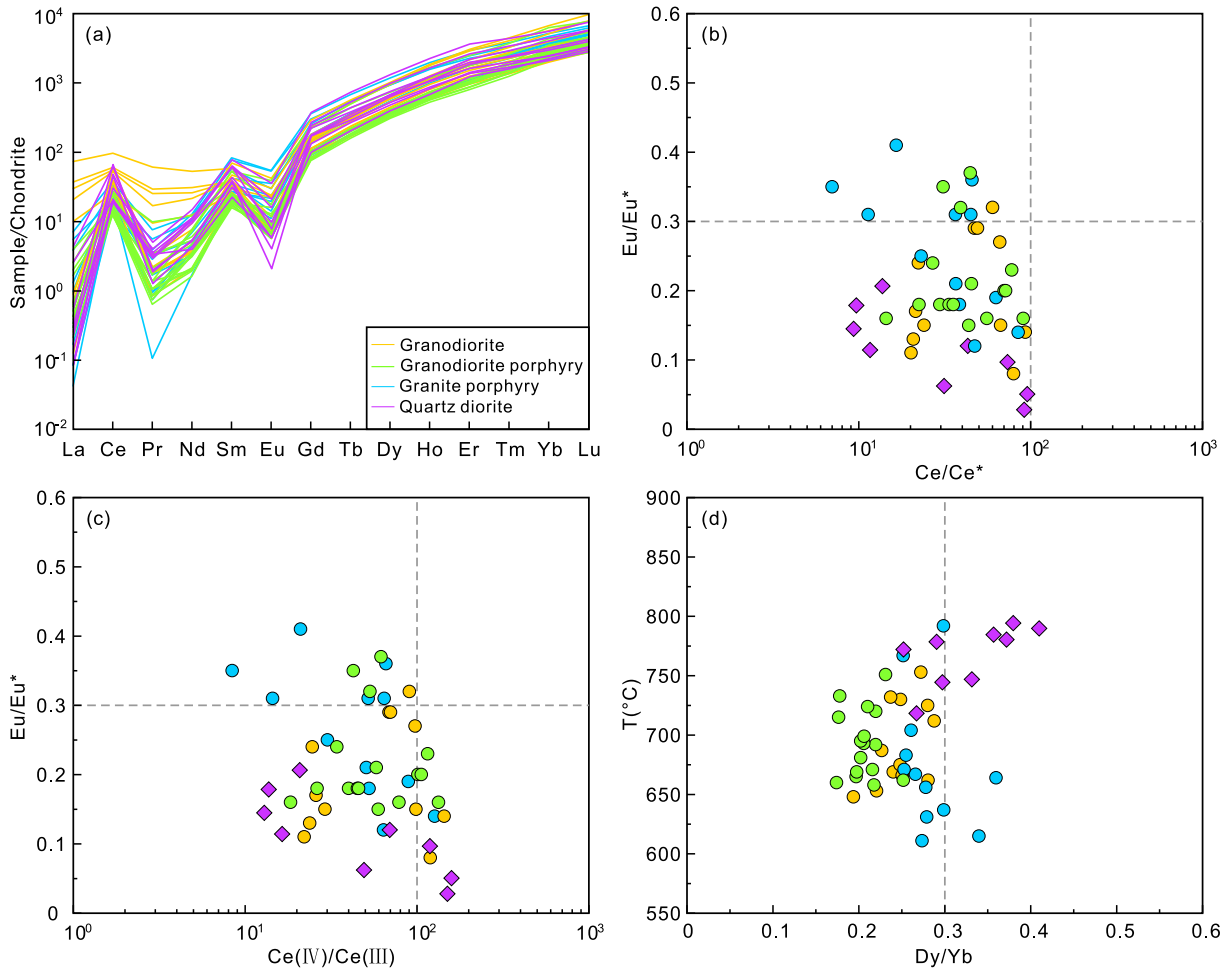

Fig. 8. (a) Chondrite-normalized REE patterns for zircons from the ore-forming suites from the Lietinggang-Leqingla deposit; Plots of (b) Ce/Ce* vs. Eu/Eu*, (c) Ce (III)/Ce (IV) vs. Eu/Eu*, (d) Dy/Yb vs. T(°C). Data sources are the same as in Fig. 6.

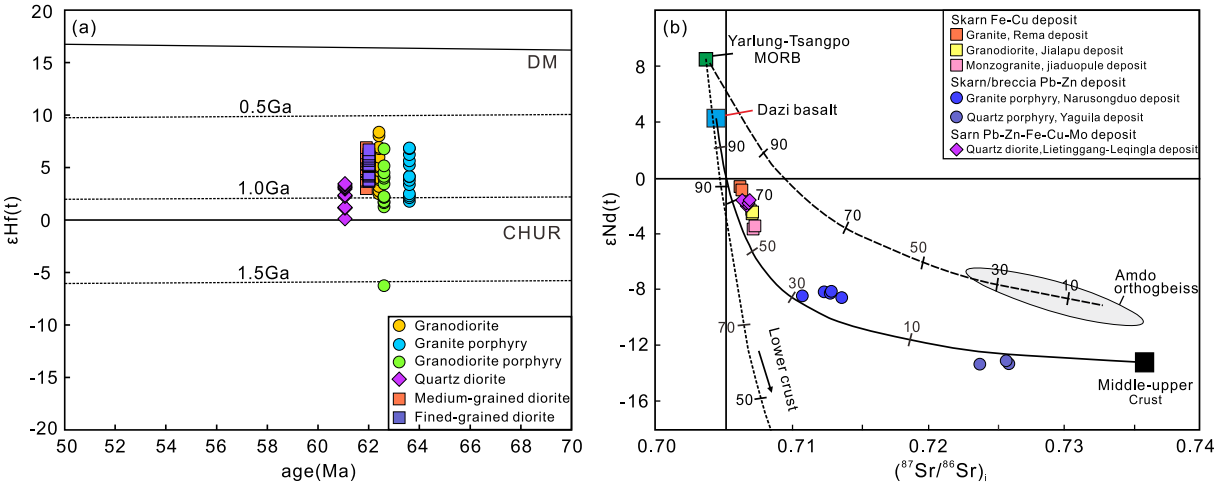

Fig. 9. (a) ε_{Hf} (t) vs. U-Pb ages for the ore-forming suites at Lietinggang-Leqingla deposit. (b) ε_{Nd} (t) vs. $(^{87}Sr/^{86}Sr)_i$ for the ore-forming rocks from deposits in the northern Gangdese polymetallic belt. The Data of the Rema, Jialapu, Jiaduopule, and Yaguila deposits are from Zheng et al. (2015), data of Narusongduo deposit are from Ji (2013). Data of the quartz diorite in Lietinggang-Leqingla deposit (this study) are shown in Table 4. Other data sources include Hou et al. (2004) for the Yarlung-Tsangpo MORB; Gao et al. (2008) for the Dazi basalt; Guynn et al. (2006) for Amdo orthogneiss; Liu et al. (2006) for the middle-upper crust in Tibet; Miller et al. (1999) for the lower crust in Tibet.

Lhasa subterrane is dominated by felsic compositions (Ji et al., 2009, 2012; Zhu et al., 2011; Zheng et al., 2015), suggesting that the intermediate-felsic rocks could not have been produced by fractional crystallization or by assimilation fractional crystallization from mantle-derived basaltic parental magmas. Melts formed directly by partial melting of crustal materials generally yield negative zircon ε_{Hf} (t) and ε_{Nd} (t) values (Jia et al., 2018; Zhang et al., 2019). This mechanism can, therefore, be precluded because all the rock types are characterized by positive ε_{Hf} (t) values (+0.1 to + 8.1) and young Hf model ages (599–1124 Ma) (Fig. 9a).

Granites formed by the reworking of supra-crustal sedimentary materials by mantle-like magmas would comprise zircons with variable ε_{Hf} (t) values (up to 10 ε units) (Kemp et al., 2007), i.e., this mechanism seems unlikely considering the limited ε_{Hf} (t) values variation of the studied samples. Consequently, we propose that the ore-forming intrusions were derived from a mantle-crust mixed source, which is confirmed by the trace element and isotopic data as will be discussed below.

The ore-forming intrusions are characterized by negative anomalies of HFSEs (e.g., Nb, Ta, Ti) and positive anomalies of LILE (Rb, Th, U, Ba), suggesting the involvement of continental crustal components in their magma source (Rudnick and Gao, 2003). Researchers have documented that the Th/U and Nb/Ta ratios can be useful for fingerprinting the source region of intrusions (Sun and McDonough, 1989; Eby et al., 1998; Gao et al., 2004). The studied ore-forming intrusions have Th/U mass ratios (3.23–9.80, average value of 4.91), as well as Nb/Ta mass ratios (10.37–20.26, average value of 12.87), which are consistent with those of the middle-upper crust (3.8–4.9 and 13.4–16.5 respectively; Rudnick and Gao, 2003). Moreover, whole rock Sr-Nd isotope and zircon Hf isotope data of the ore-forming intrusions provide further constraints on the nature of the magma source. The quartz diorites have slightly lower ε_{Nd} (t) and slightly higher $(^{87}Sr/^{86}Sr)_i$ whole-rock values (Fig. 9b), which is in agreement with the intrusive rocks being associated with regional Fe-Cu mineralization throughout the central Lhasa subterrane (Fig. 1b; Zheng et al., 2015). The ε_{Nd} (t) and $(^{87}Sr/^{86}Sr)_i$ values fall on a mixing line between the Dazi basalt and the middle-upper crust of the Lhasa terrane, indicating that the rocks were derived from a mixed mantle-crust source (Zhou et al., 2017). This is supported by zircon Hf isotopic data of the ore-forming intrusions (i.e., positive ε_{Hf} (t) values of +0.1 to +8.1 and young Hf crust model ages of 599–1124 Ma), which are similar to the young juvenile lower crustal blocks in the southern Lhasa subterranes. The identification of juvenile lower crustal blocks implies a significant mantle contribution in their formation (Hou et al., 2015). However, the ore-forming intrusions have relatively low ε_{Hf} (t) values compared to the juvenile material in the southern Lhasa subterranes (ε_{Hf} (t) > 5), implying that the contribution of mantle components to the lower crustal blocks in the central Lhasa subterrane is less than the contribution to juvenile lower crustal blocks in the southern Lhasa subterrane (Chung et al., 2005; Zhu et al., 2011; Hou et al., 2015). It is noteworthy that the granodiorite porphyry has a negative zircon ε_{Hf} (t) values of –6.3 corresponding to an old Hf crust model ages of 1522 Ma (Zhang et al., 2019), suggesting the involvement of ancient crustal components for the generation of felsic magmas. In summary, we propose that the ore-forming intrusions were generated by melting of a mixed mantle and ancient lower crustal materials. Middle to upper crustal material could also have been involved in the generation of the ore-forming intrusions of Lietinggang-Leqingla deposit.

6.2.2. *Evolution of the ore-forming intrusions*

The ore-forming intrusions show decreasing CaO, Al_2O_3, MgO, FeO, P_2O_5, and TiO_2 contents with increasing SiO_2 content, indicating that the intrusions underwent significant fractional crystallization during magma evolution. This is confirmed by the linear trends of La vs. La/Sm, Th vs. Th/La, and Rb vs. Ni (Fig. 11a-c; Allègre and Minster, 1978). The negative Eu anomalies of the ore-forming intrusions (Eu/Eu* = 0.35–0.78), combined with the linear Sr vs. Ba, Sr vs. Rb and Eu/Eu* vs. Sr/Y trends, indicate varying degrees of plagioclase fractional crystallization (Fig. 11d-f; Jing et al., 2020). The decrease of the Al_2O_3, MgO, and FeO contents with increasing SiO_2 content implies hornblende fractional crystallization (Fig. 10b-d), which is supported by the negative correlation between the Dy/Yb and Nb/Ta ratios (Fig. 11g; Jia et al., 2018). The reason for this is that the amount of hornblende fractionation will decrease the Nb/Ta ratio (Pfänder et al., 2007). Biotite has extremely high partition coefficients for V, but relatively low values for Th (Bea et al., 1994). As a peraluminous mineral, biotite fractionation will result in higher SiO_2/Al_2O_3 ratios in residual melts, while lowering V/Th ratios (Jia et al., 2018). The negative correlation between V/Th and SiO_2/Al_2O_3 ratios (Fig. 11h) suggest biotite fractionation. Furthermore, the variation of $(La/Yb)_N$ versus La (Fig. 11i) is consistent with allanite fractionation.

Generally, a granitic magma will exhibit decreasing contents of Cr, Ni, Co, Sr, Ba, Zr, and other trace elements, while the Li, Rb, and Cs increase during fractional crystallization (Gelman et al., 2014; Lee and Morton, 2015). Trace element ratios such as K/Rb, Zr/Hf and Nb/Ta

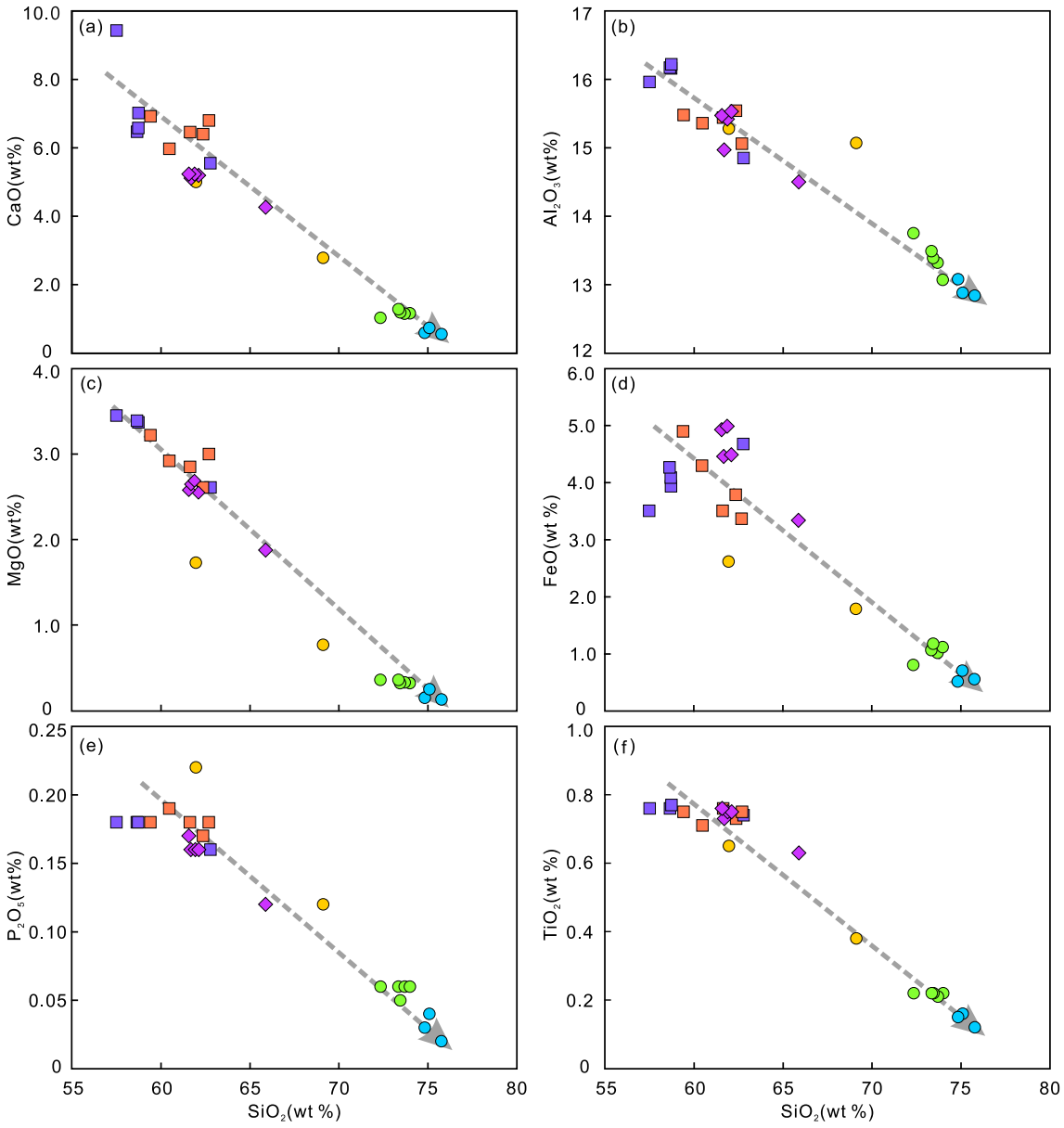

Fig. 10. Harker variation diagrams showing the major element variations in the ore-forming suites from the Lietinggang-Leqingla deposit. Data sources are the same as in Fig. 6.

have the advantage to measure the degree of fractional crystallization because of their consistent geochemical characteristics, which makes these element ratios remain constant during the magmatic evolution (Halliday et al., 1991; Green, 1995). However, these ratios would decrease when the nature of magma changed due to intense fractional crystallization (Bau, 1996; Claiborne et al., 2006; Deering and Bachmann, 2010; Dostal et al., 2015; Ballouard et al., 2016). Therefore, the Zr/Hf and Nb/Ta ratios can be used as indicators of the degree of fractional crystallization (Halliday et al., 1991; Ballouard et al., 2016). The granites in the studied deposit, the granite porphyry in the Narusongduo Pb-Zn deposit, and the quartz porphyry in the Yaguila deposit all have lower Zr/Hf mass ratios (average values of 29.01, 31.87, and 32.80, respectively) (Huang et al., 2012; Ji, 2013; Zhang et al., 2019), suggesting their highly fractionated nature (Fig. 12a). The quartz diorite in the studied deposit, the granite in the Rema Fe-Cu deposit, the granodiorite in the Jialapu deposit, and the monzogranite in the Jiaduopule deposit, on the other hand, are weakly fractionated with higher Zr/Hf mass ratios (average values of 36.10, 35.33, 40.75, and 37.60, respectively) (Yu et al., 2011; Zheng et al., 2015). Also, as shown in Fig. 12b, the ore-forming rocks of Pb-Zn deposits have relatively high $(Na_2O + K_2O)/CaO$ ratios compared with the ore-forming rocks of Fe-Cu deposits, indicating that they have undergone a significant fractionation process (Whalen et al., 1987). Therefore, it can be concluded that the ore-forming intrusions associated with Pb-Zn mineralization have experienced more intensive fractional crystallization compared to the ore-forming rocks associated with Fe-Cu mineralization from the northern Gangdese Pb-Zn-Ag-Fe-Cu-Mo-W polymetallic belt.

6.3. *Implications for the polymetallic mineralization*

The ore-forming rocks including quartz diorite, granodiorite, monzogranite, and granite that associated with the skarn Fe-Cu deposits in the NGPB are calc-alkaline and metaluminous, with lower SiO_2, and higher CaO, MgO, and FeO contents and have strong metasomatized lithospheric mantle signature (Zheng et al., 2015). Moreover, these rocks contain microgranular dioritic enclaves which have been derived

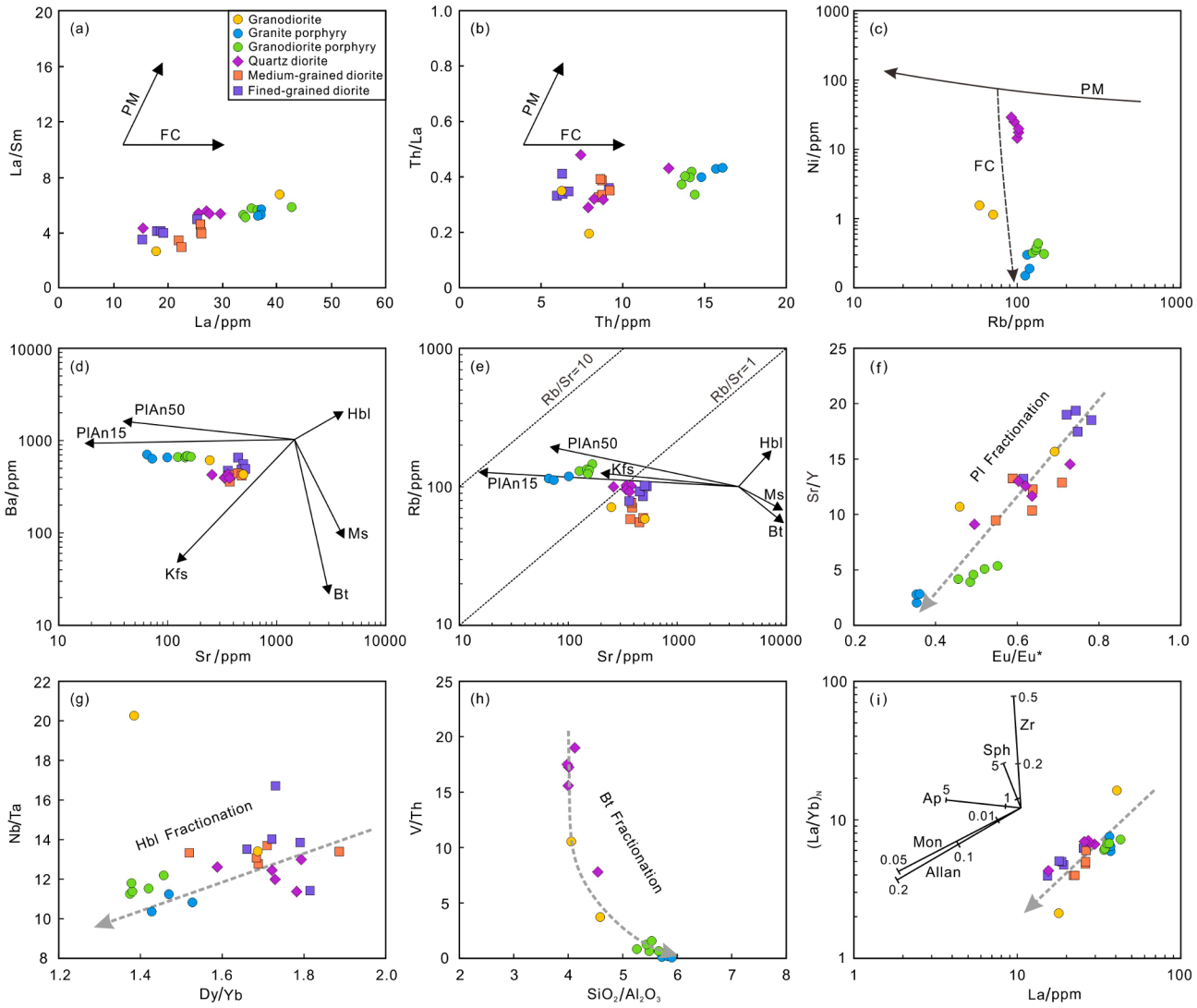

Fig. 11. Plots of (a) La/Sm vs. La, (b) Th/La vs. Th, (c) Ni vs. Rb, (d) Ba vs. Sr, (e) Rb vs. Sr, (f) Sr/Y vs. Eu/Eu*, (g) Nb/Ta vs. Dy/Yb, (h) V/Th vs. SiO_2/Al_2O_3 (Jing et al., 2020), (i) $(La/Yb)_N$ vs. La (Wu et al., 2003a). Pl: plagioclase, Kfs: K-feldspar, Hbl: hornblende, Bt: biotite, Ms: muscovite, Zr: zircon, Sph: sphene, Ap: apatite, Mon: monazite, Allan: allanite.

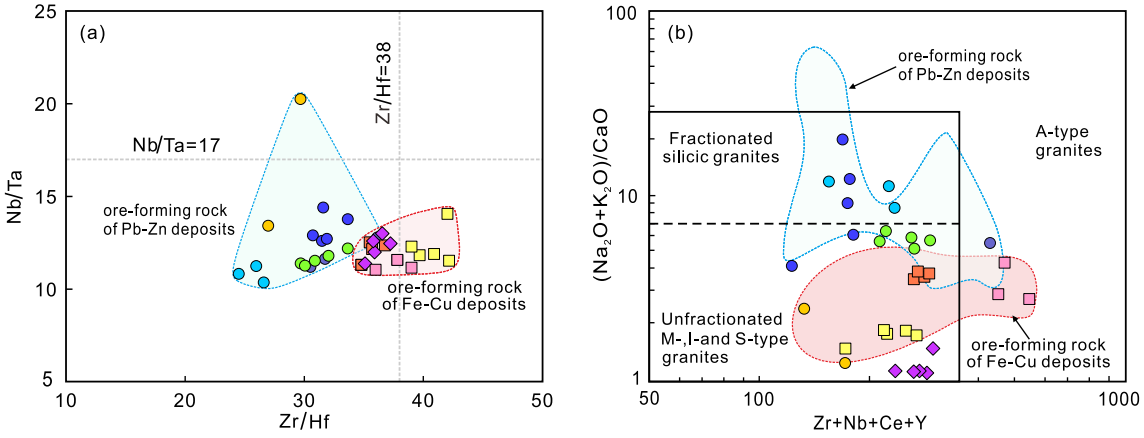

Fig. 12. Plots of (a) Nb/Ta vs. Zr/Hf (Wu et al., 2003a) and (b) $(Na_2O + K_2O)/CaO$ vs. Zr + Nb + Ce + Y (Whalen et al., 1987). The legend is the same as in Fig. 9b.

from a relatively enriched mantle source with high Cu concentrations (Hou et al., 2015; Zheng et al., 2015). Thus, the mantle-derived magmas provide Fe and Cu for the formation of the Fe-Cu ore deposits (Oyarzun et al., 2003; Zhang et al., 2019).

Lead and zinc have similar geochemical properties, i.e., they commonly coexist with each other and have a relatively high content in

the normal crust (Pb + Zn = 130 ppm; Rudnick and Gao, 2003). In addition, Pb is an incompatible element with a high abundance in the middle and upper crust (Hofmann, 1988; Gao et al., 1998). The ancient metamorphic basement in the central Lhasa terrane has relatively high Pb content (Wu et al., 2003b). Importantly, the granite-related Pb-Zn deposits in the NGPB cluster in the oldest crustal regions are developed along the margin of the old crustal block bounded by lithospheric faults (Hou et al., 2015). The addition of ancient basement materials is critical for the formation of Pb-Zn ore deposits (Zheng et al., 2015). It is noteworthy that the ore-forming rocks related to Pb-Zn deposits have experienced more extensive fractional crystallization compared to the ore-forming rocks of the Fe-Cu deposits in the NGPB. Continuous magma differentiation can cause enrichment of incompatible elements up to 30 times (Lee and Morton, 2015). Therefore, the Pb-Zn mineralization in the NGPB was controlled by presence of ancient basement materials and extensive fractional crystallization.

The Lietinggang-Leqingla deposit is one of the unique typical skarn polymetallic deposits with Pb-Zn-Fe-Cu-(Mo) mineralization in the central Lhasa subterrane. This deposit requires magmatic conditions to form Fe-Cu and Pb-Zn at the same time. The ore-forming rocks related to mineralization include granodiorite, granite porphyry, granodiorite porphyry, quartz diorite, medium-grained diorite, and fine-grained diorite. Most geochemical characteristics indicate that the intermediate intrusions are similar to the ore-forming rocks associated with Fe-Cu deposits in the NGPB (Figs. 9, 12). This implies that the magmas were derived from partial melting of lithospheric mantle mixed with the rejuvenated lower crustal melts (Zheng et al., 2015). Such a mixed crust-mantle magmatic source comprising ore metals underwent weak fractional crystallization during the ascent process, followed by skarn Fe-Cu mineralization formed near the surface at the contact with carbonate rocks. However, the geochemical characteristics of felsic intrusions are consistent with the ore-forming rocks related to Pb-Zn deposits in the NGPB (Fig. 12). Thus, these rocks were formed by melting of a mantle-derived basaltic magmas mixed with old lower to upper crustal material. During the ascent and emplacement of the melts into shallow crustal levels, the magma underwent extensive fractional crystallization, and formed skarn Pb-Zn mineralization in limestone.

7. Conclusions

The conclusions of this study are the following:

(1) The newly identified quartz diorite associated with mineralization at Lietinggang-Leqingla deposit was formed at 61.06 ± 0.63 Ma, which is coeval with the mineralization-related granodiorite, granite porphyry, granodiorite porphyry, medium-grained diorite, and fine-grained diorite.
(2) The intermediate intrusions associated with Fe-Cu mineralization were derived from partial melting of lithospheric mantle mixed with the rejuvenated lower crustal melts, and underwent weakly fractional crystallization during upwelling.
(3) The felsic intrusions associated with Pb-Zn mineralization were formed by melting a mantle-derived basaltic magmas with old lower crust component contributions, and experienced extensive crystal fractionation.
(4) The Lietinggang-Leqingla polymetallic deposit can be explained by the simultaneous formation of the ore-forming rocks related to Fe-Cu and Pb-Zn mineralization.

Declaration of Competing Interest

The authors declare that they have no known competing financial interests or personal relationships that could have appeared to influence the work reported in this paper.

Acknowledgments

We are grateful to the staff of the Tianguansanqin Company, Jinshen Zhou, Linyuan Zhang, and Yuxuan Zhang for their assistance with fieldwork. Chao Yu from the Institute of Geology, Chinese Academy of Geological Sciences is thanked for helping with zircon LA-ICP-MS U-Pb analyses. Tianfang Ma and Limin Zhou from the National Research Center for Geoanalysis are thanked for whole rock geochemical analyses and Lu-Hf isotopic analyses. Ping Xiao from University of Science and Technology of China is thanked for Sr-Nd isotopic analyses. Funding for this research was provided by the National Natural Science Foundation of China (Nos. 41922022, 91962105, 92162322, and 42072107), the Key Laboratory of Deep-Earth Dynamics of Ministry of Natural Resources (grant numbers J1901-16), the Strategic Priority Research Program of Chinese Academy of Sciences, China (No. XDA20070304), the Second Tibetan Plateau Scientific Expedition and Research (2021QZKK0304), the Basic Scientific Research Foundation of the Institute of Geology, Chinese Academy of Geological Sciences (No. J2105), and the IGCP-662 program.

References

Allègre, C.J., Minster, J.F., 1978. Quantitative models of trace element behavior in magmatic processes. Earth Planet. Sci. Lett. 38, 1–25.
Ballard, J.R., Palin, M.J., Campbell, I.H., 2002. Relative oxidation states of magmas inferred from Ce (IV)/Ce (III) in zircon: Application to porphyry copper deposits of northern Chile. Contrib. Mineral. Petrol. 144, 347–364.
Ballouard, C., Poujol, M., Boulvais, P., Branquet, Y., Tartèse, R., Vigneresse, J.L., 2016. Nb-Ta fractionation in peraluminous granites: A marker of the magmatic-hydrothermal transition. Geology 44, 231–234.
Bau, M., 1996. Controls on the fractionation of isovalent trace elements in magmatic and aqueous systems: Evidence from Y/Ho, Zr/Hf, and lanthanide tetrad effect. Contrib. Mineral. Petrol. 123, 323–333.
Bea, F., Pereira, M.D., Stroh, A., 1994. Mineral/leucosome trace-element partitioning in a peraluminous migmatite (a laser ablation-ICP-MS study). Chem. Geol. 117, 291–312.
Burnham, A., Berry, A., Halse, H., Schofield, P., Cibin, G., Mosselmans, J., 2015. The oxidation state of europium in silicate melts as a function of oxygen fugacity, composition and temperature. Chem. Geol. 411, 248–259.
Chang, Z.S., Shu, Q.H., Meinert, L.D., 2019. Skarn Deposits of China. Econ. Geol. SEG Special Publications. 22, 189–234.
Chappell, B.W., White, A.J.R., 1992. I- and S-type granites in the Lachlan Fold Belt. Geol. Soc. Am. Spec. Papers 272, 1–26.
Chen, F.K., Li, X.H., Wang, X.L., Li, Q.L., Siebel, W., 2007. Zircon age and Nd-Hf isotopic composition of the Yunnan Tethyan belt, southwestern China. Int. J. Earth Sci. 96, 1179–1194.
Chen, F.K., Zhu, X.Y., Wang, W., Wang, F., Hieu, P.T., Siebel, W., 2009. Single-grain detrital muscovite Rb-Sr isotopic composition as an indicator of provenance for the Carboniferous sedimentary rocks in northern Dabie, China. Geochem. J. 43, 257–273.
Chu, M.F., Chung, S.L., Song, B., Liu, D., O'Reilly, S.Y., Pearson, N.J., Ji, J., Wen, D.-J., 2006. Zircon U-Pb and Hf isotope constraints on the Mesozoic tectonics and crustal evolution of southern Tibet. Geology 34, 745–748.
Chung, S.L., Liu, D.Y., Ji, J., Chu, M.F., Lee, H.Y., Wen, D.J., Lo, C.H., Lee, T.Y., Qian, Q., Zhang, Q., 2003. Adakites from continental collision zones: Melting of thickened lower crust beneath southern Tibet. Geology 31, 1021–1024.
Chung, S.L., Chu, M.F., Zhang, Y.Q., Xie, Y.W., Lo, C.H., Lee, T.Y., Lan, C.Y., Li, X.H., Zhang, Q., Wang, Y.Z., 2005. Tibetan tectonic evolution inferred from spatial and temporal variations in post-collisional magmatism. Earth Sci. Rev. 68, 173–196.
Claiborne, L.L., Miller, C.F., Walker, B.A., Wooden, J.L., Mazdab, F.K., Bea, F., 2006. Tracking magmatic processes through Zr/Hf ratios in rocks and Hf and Ti zoning in zircons: An example from the Spirit Mountain batholith, Nevada. Mineral Mag 70, 517–543.
Danyushevsky, L.V., Falloon, T.J., Crawford, A.J., Tetroeva, S.A., Leslie, R.L., Verbeeten, A., 2008. High-Mg adakites from Kadavu Island Group, Fiji, southwest Pacific: Evidence for the mantle origin of adakite parental melts. Geology 36, 499–502.
DeCelles, P.G., Gehrels, G.E., Najiman, Y., Martin, A., Carter, A., Garzanti, E., 2004. Detrital geochronology and geochemistry of Cretaceous early Miocene strata of Nepal: Implications for timing and diachroneity of initial Himalayan orogenies. Earth Planet. Sci. Lett. 227, 313–330.
Deering, C.D., Bachmann, O., 2010. Trace element indicators of crystal accumulation in silicic igneous rocks. Earth Planet. Sci. Lett. 297, 324–331.
Dilles, J.H., Kent, A.J.R., Wooden, J.L., Tosdal, R.M., Koleszar, A., Lee, R.G., Farmer, L.P., 2015. Zircon compositional evidence for sulfur-degassing from ore-forming arc magmas. Econ. Geol. 110, 241–251.
Dong, X., Zhang, Z.M., Santosh, M., 2010. Zircon U-Pb chronology of the Nyingtri Group, Southern Lhasa Terrane, Tibetan Plateau: Implications for Grenvillian and Pan-African Provenance and Mesozoic-Cenozoic Metamorphism. J. Geol. 118, 677–690.

Dostal, J., Kontak, D.J., Gerel, O., Gregory Shellnutt, J., Fayek, M., 2015. Cretaceous ongonites (topaz-bearing albite-rich microleucogranites) from Ongon Khairkhan, Central Mongolia: Products of extreme magmatic fractionation and pervasive metasomatic fluid: Rock interaction. Lithos 236–237, 173–189.
Drummond, M.S., Defant, M.J., 1990. A model for trondhjemite-tonalite-dacite genesis and crustal growth via slab melting: Archean to modern comparisons. J. Geophys. Res. 95, 21503–21521.
Duchesne, J.C., Berza, T., Liégeois, J.P., Auwera, J.V., 1998. Shoshonitic liquid line of descent from diorite to granite: the Late Precambrian post-collisional Tismana pluton (South Carpathians, Romania). Lithos 45, 281–303.
Eby, G.N., Woolley, A.R., Din, V., Platt, G., 1998. Geochemistry and petrogenesis of Nepheline Syenite: Kasungu-Chipala, Ilomba, and Ulindi Nepheline Syenite intrusions, North Nyasa Alkaline Province. Malawi. J. Petrol. 39, 1405–1424.
Einaudi, M.T., Meinert, L.D., Newberry, R.J., 1981. Skarn deposits. Economic geology 75th anniversary volume. 317–391.
Einaudi, M.T., 1982. Descriptions of skarn associated with porphyry copper plutons, southwestern North America. In: Titley, S.R. (Ed.), Advances in Geology of the Porphyry Copper Deposits, Southwestern North America: Tucson. University of Arizona Press, pp. 139–184.
Ferry, J.M., Watson, E.B., 2007. New thermodynamic models and revised calibrations for the Ti-in-zircon and Zr-in-rutile thermometers. Contrib. Miner. Petrol. 154, 429–437.
Fu, Q., Yang, Z.S., Zheng, Y.C., Huang, K.X., Duan, L.F., 2014. Ar-Ar age of phlogopite from Longmala copper-iron-lead-zinc deposit in Tibet, and its geodynamic significance. Acta Petrol. Mineral. 33, 283–293 in Chinese with English abstract.
Fu, Q., Xu, B., Zheng, Y.C., Yang, Z.S., Hou, Z.Q., Huang, K.X., Liu, Y.C., Zhang, C., Zhao, L., 2017. Two episodes mineralization in the Mengya'a deposit and implication for the evolution and intensity of Pb–Zn–(Ag) mineralization in the Lhasa terrane, Tibet. Ore Geol. Rev. 90, 877–896.
Gao, S., Luo, T.C., Zhang, B.R., 1998. Chemical composition of the continental crust as revealed by studies in East China. Geochim. Cosmochim. Acta 62, 1959–1975.
Gao, S., Rudnick, R.L., Yuan, H.L., Liu, X.M., Liu, Y.S., Xu, W.L., Ling, W.L., Ayers, J., Wang, X.C., Wang, Q.H., 2004. Recycling lower continental crust in the North China craton. Nature 432, 892–897.
Gao, Y.F., Hou, Z.Q., Kamber, B.S., Wei, R.H., Meng, X.J., Zhao, R., 2007. Adakite-like porphyries from the southern Tibetan continental collision zones: evidence for slab melt metasomatism. Contrib. Mineral. Petrol. 153, 105–120.
Gao, Y.F., Wei, R.H., Hou, Z.Q., Tian, S.H., Zhao, R.S., 2008. Eocene high-MgO volcanism in southern Tibet, new constraints for mantle source characteristics and deep processes. Lithos 105, 63–72.
Gao, Y.M., Chen, Y.C., Tang, J.X., Li, C., Li, X.F., Gao, M., Cai, Z.C., 2011. Re-Os dating of molybdenite from the Yaguila porphyry molybdenum deposit in Gongbo'gyamda area, Tibet, and its geological significance. Geol. Bull. China 30, 1027–1036 in Chinese with English abstract.
Gelman, S.E., Deering, C.D., Bachmann, O., Huber, C., Gutiérrez, F.J., 2014. Identifying the crystal graveyards remaining after large silicic eruptions. Earth Planet. Sci. Lett. 403, 299–306.
Green, T.H., 1995. Significance of Nb/Ta as an indicator of geochemical processes in the crust-mantle system. Chem. Geol. 120, 347–359.
Griffin, W., Pearson, N., Belousova, E., Jackson, S., Van Achterbergh, E., O'Reilly, S.Y., Shee, S., 2000. The Hf isotope composition of cratonic mantle: LAM-MC-ICPMS analysis of zircon megacrysts in kimberlites. Geochim. Cosmochim. Acta 64, 133–147.
Griffin, W., Wang, X., Jackson, S., Pearson, N., O'Reilly, S.Y., Xu, X., Zhou, X., 2002. Zircon chemistry and magma mixing, SE China: in-situ analysis of Hf isotopes, Tonglu and Pingtan igneous complexes. Lithos 61, 237–269.
Grove, T.L., Donnelly-Nolan, J.M., Housh, T., 1997. Magmatic processes that generated the rhyolite of Glass Mountain, Medicine Lake volcano, N. California. Contrib. Mineral. Petrol. 127, 205–223.
Guynn, J.H., Kapp, A., Heizler, M., Gehrels, G., Ding, L., 2006. Tibetan basement rocks near Amdo reveal "missing" Mesozoic tectonism along the Bangong suture, central Tibet. Geology 34, 505–508.
Halliday, A.N., Davidson, J.P., Hildreth, W., Holden, P., 1991. Modelling the petrogenesis of high Rb/Sr silicic magmas. Chem. Geol. 92, 107–114.
Harris, N.B.W., Inger, S., Xu, R.H., 1990. Cretaceous plutonism in central Tibet: An example of post-collision magmatism? J. Volcanol. Geotherm. Res. 44, 21–32.
Hezarkhhani, A., 2006. Petrology of the intrusive rocks within the Sungun porphyry copper deposit, Azerbaijan, Iran. J. Asian Earth Sci. 27, 326–340.
Hofmann, A.W., 1988. Chemical differentiation of the Earth: the relationship between mantle, continental crust, and oceanic crust. Earth Planet. Sci. Lett. 90, 297–314.
Hou, Z.Q., Gao, Y.F., Qu, X.M., Rui, Z.Y., Mo, X.X., 2004. Origin of adakitic intrusives generated during mid-Miocene east–west extension in southern Tibet. Earth Planet. Sci. Lett. 220, 139–155.
Hou, Z.Q., Yang, Z.S., Xu, W.Y., Mo, X.X., Ding, L., Gao, Y.F., Dong, F.L., Li, G.M., Qu, X. M., Zhao, Z.D., Jiang, S.H., Meng, X.J., Li, Z.Q., Qin, K.Z., Yang, Z.M., 2006. Metallogenesis in Tibetan collisional orogenic belt: I. Mineralization in main collisional orogenic setting. Miner. Deposits 25, 337–358 in Chinese with English abstract.
Hou, Z.Q., Cook, N.J., 2009. Metallogenesis of the Tibetan collisional orogen: a review and introduction to the special issue. Ore Geol. Rev. 36, 2–24.
Hou, Z.Q., Zheng, Y.C., Yang, Z.M., Rui, Z.Y., Zhao, Z.D., Jiang, S.H., Qu, X.M., Sun, Q.Z., 2013. Contribution of mantle components within juvenile lower-crust to collisional zone porphyry Cu systems in Tibet. Miner. Deposita 48, 173–192.
Hou, Z.Q., Duan, L.F., Lu, Y.J., Zheng, Y.C., Zhu, D.C., Yang, Z.M., Yang, Z.S., Wang, B. D., Pei, Y.R., Zhao, Z.D., McCuaig, T.C., 2015. Lithospheric architectures of the Lhasa Terrane and its control on ore deposits in Himalayan-Tibetan orogen. Econ. Geol. 110, 1541–1575.
Hou, Z.Q., Zheng, Y.C., Lu, Z.W., Xu, B., Wang, C.M., Zhang, H.R., 2021. Growth, thickening and evolution of the thickened crust of the Tibet Plateau. Acta Geol. Sinica 94, 2797–2815 in Chinese with English abstract.
Huang, K.X., Zheng, Y.C., Zhang, S., Li, W., Sun, Q.Z., Li, Q.Y., Liang, W., Fu, Q., Hou, Z. Q., 2012. LA-ICP-MS zircon U-Pb dating of two types of porphyry in the Yaguila mining area, Tibet. Acta Petrol. Mineral. 31, 348–360 in Chinese with English abstract.
Ji, W.Q., Wu, F.Y., Chung, S.L., Li, J.X., Liu, C.Z., 2009. Zircon U-Pb geochronology and Hf isotopic constraints on petrogenesis of the Gangdese batholith, southern Tibet. Chem. Geol. 262, 229–245.
Ji, W.Q., Wu, F.Y., Liu, C.Z., Chung, S.L., 2012. Early Eocene crustal thickening in southern Tibet: new age and geochemical constraints from the Gangdese batholith. J. Asian Earth Sci. 53, 82–95.
Ji, X.H., 2013. Study on Geology, Geochemistry and Genesis of Narusongduo Lead-zinc Deposit, Tibet. China University of Geosciences, Beijing. PhD dissertation.
Jia, L.H., Mao, J.W., Liu, P., Li, Y., 2018. Petrogenesis of the late Early Cretaceous granodiorite–Quartz diorite from eastern Guangdong, SE China: Implications for tectono–magmatic evolution and porphyry Cu-Au-Mo mineralization. Lithos 304–307, 388–411.
Jing, Y., Ji, Z., Ge, W.C., Dong, Y., Yang, H., Bi, J.H., 2020. Middle-late permian I-type granitoids from the Diaobingshan region in the northern margin of the North China Craton: insight into southward subduction of the Paleo-Asian Ocean. Int. Geol. Rev. 63, 357–379.
Kemp, A.I.S., Hawkesworth, C.J., Foster, G.L., Paterson, B.A., Woodhead, J.D., Hergt, J. M., Gray, C.M., Whitehouse, M.J., 2007. Magmatic and crustal differentiation history of granitic rocks from Hf-O isotopes in zircon. Science 315, 980–983.
Kloppenburg, A., Grotcott, J., Hutchinson, D., 2012. Structural setting and synplutonic fault kinematics of a Cordilleran Cu-Au-Mo porphyry mineralization system, Bingham mining district, Utah. Econ. Geol. 105, 743–761.
Lee, C.T.A., Morton, D.M., 2015. High silica granites: terminal porosity and crystal settling in shallow magma chambers. Earth Planet. Sci. Lett. 409, 23–31.
Li, H.M., Wang, D.H., Li, L.X., Chen, J., Yang, X.Q., Liu, M.J., 2012. Metallogeny of iron deposits and resource potential of major iron minerogenetic units in China. Geol. China 39, 559–580 in Chinese with English abstract.
Li, X.F., Wang, C.Z., Mao, W., Xu, Q.H., Liu, Y.H., 2014. The fault-controlled skarn W-Mo polymentallic mineralization during the main India-Eurasia collision: example form Hahaigang deposit of Gangdese metallogenic belt of Tibet. Ore Geol. Rev. 58, 27–40.
Liu, Q.S., Jiang, W., Jian, P., Yem, P.S., Wu, Z.H., Chen, D.G., 2006. Zirocn SHRIMP U-Pb age and petrochemical and geochemical features of Mesozoic muscovite monzonitic granite at Ningzhong, Tibet. Acta Petrol. Sin. 22, 643–652 in Chinese with English abstract.
Loader, M.A., Wilkinson, J.J., Armstrong, R.N., 2017. The effect of titanite crystallisation on Eu and Ce anomalies in zircon and its implications for the assessment of porphyry Cu deposit fertility. Earth Planet. Sci. Lett. 472, 107–119.
Lu, Y.J., Loucks, R.R., Fiorentini, M., McCuaig, T.C., Evans, N.J., Yang, Z.M., Hou, Z.Q., Kirkland, C.L., Parra-Avila, L.A., Kobussen, A., 2016. Zircon composition as a pathfnder for porphyry Cu ± Mo ± Au deposits: Society of Economic Geologists. Special Publication 19, 329–347.
Ma, W., Yang, Z.S., Hou, Z.Q., Li, Z.Q., Fei, F., Fu, Q., Duan, L.F., Zhao, X.Y., Pei, Y.R., Han, C.H., Liu, Y.C., 2015. Zircon U-Pb dating and geochemical characteristics of metallogenetic rock from the Lietinggang-Leqingla Fe-Cu-Pb-Zn deposit in Tibet. Acta Geol. Sinica 89, 1655–1672 in Chinese with English abstract.
Ma, W., Liu, Y.C., Yang, Z.S., Li, Z.Q., Zhao, X.Y., Fei, F., 2017. Alteration, mineralization, and genesis of the Lietinggang-Leqingla Pb-Zn-Fe-Cu-Mo skarn deposit, Tibet, China. Ore Geol. Rev. 90, 897–912.
Ma, W., Liu, Y.C., Yang, Z.S., Li, Z.Q., Zhao, X.Y., Yue, L.L., 2019. Characteristics of ore forming fluids of Lietinggang-Leqingla Pb-Zn-Fe-Cu-Mo polymetallic deposit in Tibetan: Evidence from fluid inclusions and stable isotope compositions. Earth Sci. 44, 1957–1973 in Chinese with English abstract.
Ma, W., Liu, Y.C., Yang, Z.S., Li, Z.Q., Zhao, X.Y., Yue, L.L., Tang, B.L., 2020. Sulfide Re-Os and Rb-Sr ages of Lietinggang-Leqingla Pb-Zn-Fe-Cu-Mo deposit in Tibet and its geological significance. Miner. Deposits 39, 80–96 in Chinese with English abstract.
Maher, K.C., 2010. Skarn alteration and mineralization at Coroccohuayco, TIntaya District, Peru. Econ. Geol. 105, 263–283.
Meng, X.J., Hou, Z.Q., Ye, P.S., Yang, Z.S., Li, Z.Q., Gao, Y.F., 2007. Characteristics and ore potentiality of Gangdese silver-polymetallic mineralization belt in Tibet. Miner. Deposits 26, 153–162 in Chinese with English abstract.
Meinert, L.D., 1995. Compositional variation of igneous rocks associated with skarn deposits-chemical evidence for a genetic connection between petrogenesis and mineralization: Mineralogical Association of Canada Short Course Series 23, 401–418.
Meinert, L.D., 2005. World skarn deposit. Society of Economic Geologists, Inc. Economic Geology 100th Anniversary Volume. 299–336.
Miller, C., Schuster, R., Klötzli, U., Frank, W., Purtscheller, F., 1999. Post-collisional potassic and ultrapotassic magmatism in SW Tibet, geochemical and Sr–Nd–Pb–O isotopic constraints for mantle source characteristics and petrogenesis. J. Petrol. 40, 1399–1424.
Mo, X.X., Zhao, Z.D., Deng, J.F., Dong, G.C., Zhou, S., 2003. Response of volcanism to the India-Asia collision. Earth Sci. Front. 10, 135–148 in Chinese with English abstract.
Mo, X.X., Dong, G.C., Zhao, Z.D., Guo, T.Y., Wang, L.L., Chen, T., 2005. Timing of magma mixing in the Gangdisè magmatic belt during the India-Asia collision, Zircon SHRIMP U-Pb dating. Acta Geol. Sinica 79, 66–76.
Mo, X.X., Hou, Z.Q., Niu, Y.L., Dong, G.C., Qu, X.M., Zhao, Z.D., Yang, Z.M., 2007. Mantle contributions to crustal thickening during continental collision, evidence from Cenozoic igneous rocks in southern Tibet. Lithos 96, 225–242.

Newberry, R.J., Swanson, S.E., 1986. Scheelite skarn granitoids: An evaluation of the roles of magmatic source and process. Ore Geol. Rev. 1, 57–81.
Oyarzun, R., Oyarzun, J., Menard, J.J., Lillo, J., 2003. The Cretaceous iron belt of northern Chile: Role of oceanic plates, a superplume event and a major shear zone. Miner. Deposita 38, 640–646.
Pan, G.T., Ding, J., Yao, D.S., Wang, L.Q., 2004. Guidebook of 1:1,500,000 Geologic Map of the Qinghai-Xizang (Tibet) Plateau and Adjacent Areas: Chengdu, China, Cartographic Publishing House 1–148 (in Chinese).
Paton, C., Woodhead, J.D., Hellstrom, J.C., Hergt, J.M., Greig, A., Maas, R., 2010. Improved laser ablation U-Pb zircon geochronology through robust downhole fractionation correction. Geochem. Geophys. Geosyst. 11, Q0AA06.
Pfänder, J.A., Münker, C., Stracke, A., Mezger, K., 2007. Nb/Ta and Zr/Hf in ocean island basalts-implications for crust-mantle differentiation and the fate of Niobium. Earth Planet. Sci. Lett. 254, 158–172.
Qiu, J.T., Yu, X.Q., Santosh, M., Zhang, D.H., Chen, S.Q., Li, P.J., 2013. Geochronology and magmatic oxygen fugacity of the Tongcun molybdenum deposit, northwest Zhejiang, SE China. Miner. Deposita. 48, 545–556.
Richards, J.P., 2009. Postsubduction porphyry Cu-Au and epithermal Au deposits: products of remelting of subduction-modified lithosphere. Geology 37, 247–250.
Richards, J.P., 2011. Magmatic to hydrothermal metal fluxes in convergent and collided margins. Ore Geol. Rev. 40, 1–26.
Rickwood, P.C., 1989. Boundary lines within petrologic diagrams which use oxides of major and minor elements. Lithos 22, 247–263.
Rollinson, H.R., 1993. In: Using Geochemical Data: Evaluation, Presentation. Interpretation. Longman, Essex, pp. 171–214.
Rudnick, R., Gao, S., 2003. Composition of the continental crust. In: Holland, H.D., Turekian, K.K (Eds.), Treatise on Geochemistry. Elsevier-Pergamon, Oxford, pp. 1–64.
Samson, I.M., Williams-Jones, A.E., Ault, K.M., Gagnon, J.E., Fryer, B.J., 2008. Source of fluids forming distal Zn-Pb-Ag skarns: evidence from laser ablation-inductively coupled plasma-mass spectrometry analysis of fluid inclusions from El Mochito, Honduras. Geology 36, 947–950.
Shu, Q.H., Chang, Z.S., Hammerli, J., Lai, Y., Huizenga, J.M., 2017. Composition and evolution of fluids forming the Baiyinnuo'er Zn-Pb skarn deposit, northeastern China: Insights from laser ablation ICP-MS study of fluid inclusions. Econ. Geol. 112, 1441–1460.
Sisson, T.W., Ratajeski, K., Hankins, W.B., Glazner, A.F., 2005. Voluminous granitic magmas from common basaltic sources. Contrib. Miner. Petrol. 148, 635–661.
Streck, M.J., Leeman, W.P., Chesley, J., 2007. High-magnesian andesite from Mount Shasta: A product of magma mixing and contamination, not a primitive mantle melt. Geology 35, 351–354.
Sun, S.S., Mcdonough, W.F., 1989. Chemical and isotopic systematics of oceanic basalts: implications for mantle composition and processes. Geol. Soc. London Spec. Publ. 42, 313–345.
Wang, B.D., Xu, J.F., Chen, J.L., Zhang, X.G., Wang, L.Q., Xia, B.B., 2010. Petrogenesis and geochronology of the ore-bearing porphyritic rocks in Tangbula porphyry molybdenum–copper deposit in the eastern segment of the Gangdese metallogenic belt. Acta Petrol. Sin. 26, 1820–1832 in Chinese with English abstract.
Wang, L.Q., Tang, J.X., Bagas, L., Wang, Y., Lin, X., Li, Z., Li, Y.B., 2017. Early Eocene Longmala skarn Pb-Zn-Cu deposit in Tibet, China: Geochemistry, fluid inclusions, and H-O-S-Pb isotopic compositions. Ore Geol. Rev. 88, 99–115.
Wang, L.Q., Tang, J.X., Yang, Y., Li, Z., Lin, X., 2018. Zircon U-Pb geochronology, geochemistry, and S-Pb isotopic compositions of the Lietinggang iron polymetallic deposit, Tibet, China. Ore Geol. Rev. 98, 62–79.
Wang, Y., Zhu, X.K., Mao, J.W., Li, Z.H., Cheng, Y.B., 2011. Iron isotope fractionation during skarn-type metallogeny: a case study of Xinqiao Cu-S-Fe-Au deposit in the Middle-Lower Yangtze valley. Ore Geol. Rev. 43, 194–202.
Wang, R., Richards, J.P., Zhou, L.M., Hou, Z.Q., Stern, R.A., Creaser, R.A., Zhu, J.J., 2015. The role of Indian and Tibetan lithosphere in spatial distribution of Cenozoic magmatism and porphyry Cu-Mo deposits in the Gangdese belt, southern Tibet. Earth Sci. Rev. 150, 68–94.
Watson, E.B., Wark, D.A., Thomas, J.B., 2006. Crystallization thermometers for zircon and rutile. Contrib. Miner. Petrol. 151, 413–433.
Whalen, J.B., Currie, K.L., Chappell, B.W., 1987. A-type granites: geochemical characteristics, discrimination and petrogenesis. Contrib. Miner. Petrol. 95, 407–419.
Wu, F.Y., Jahn, B.M., Wilde, S.A., Lo, C.H., Yui, T.F., Lin, Q., Sun, D.Y., 2003a. Highly fractionated I-type granites in NE China (I): Geochronology and petrogenesis. Lithos 66, 241–273.
Wu, F.Y., Yang, Y.H., Xie, L.W., Yang, J.H., Xu, P., 2006. Hf isotopic compositions of the standard zircons and baddeleyites used in U-Pb geochronology. Chem. Geol. 234, 105–126.
Wu, Z.H., Ye, P.S., Hu, D.G., Liu, Q.S., 2003b. Thrust system of the north Lhasa block. Geol. Rev. 49, 74–80 in Chinese with English abstract.
Xu, B., Hou, Z.Q., Zheng, Y.C., Wang, R., He, M.Y., Zhou, L.M., Yang, Y., 2017. In situ elemental and isotopic study of diorite intrusions: implication for Jurassic arc magmatism and porphyry Cu-Au mineralization in southern Tibet. Ore Geol. Rev. 90, 1063–1077.
Xu, B., Hou, Z., Griffin, W.L., Zheng, Y., Wang, T., Guo, Z., Hou, J., Santosh, M., O'Reilly, S.Y., 2021a. Cenozoic lithospheric architecture and metallogenesis in southeastern Tibet. Earth Sci. Rev. 214, 103472.
Xu, B., Hou, Z.Q., Griffin, W.L., Lu, Y., Belousova, E., Xu, J.F., O'Reilly, S.Y., 2021b. Recycled volatiles determine fertility of porphyry deposits in collisional settings. Am. Mineral. 106, 656–661.
Yang, Z.M., Lu, Y.J., Hou, Z.Q., Chang, Z.S., 2015. High-Mg Diorite from Qulong in Southern Tibet: Implications for the Genesis of Adakite-like Intrusions and Associated Porphyry Cu Deposits in Collisional Orogens. J. Petrol. 56, 227–254.
Yang, Z.M., Hou, Z.Q., Chang, Z.S., Li, Q.Y., Liu, Y.F., Qu, H.C., Sun, M.Y., Xu, B., 2016. Cospatial Eocene and Miocene granitoids from the Jiru Cu deposit in Tibet: Petrogenesis and implications for the formation of collisional and postcollisional porphyry Cu systems in continental collision zones. Lithos 245, 243–257.
Yin, A., Harrison, T.M., 2000. Geologic evolution of the Himalayan-Tibetan orogen. Annu. Rev. Earth Planet. Sci. 28, 211–280.
Yu, Y.S., Yang, Z.S., Duo, J., Hou, Z.Q., Tian, S.H., Meng, X.J., Liu, H.F., Zhang, J.S., Wang, H.P., Liu, Y.C., 2011. Age and petrogenesis of magmatic rocks from Jiaduopule skarn Fe-Cu deposit in Tibet: evidence from zircon SHRIMP U-Pb dating, Hf isotope and REE. Miner. Depos. 30, 420–434 in Chinese with English abstract.
Zarasvandi, A., Rezaei, M., Sadeghi, M., Lentz, D., Adelpour, M., Pourkaseb, H., 2015. Rare earth element signatures of economic and sub-economic porphyry copper systems in Urumieh-Dokhtar Magmatic Arc (UDMA), Iran. Ore Geol. Rev. 70, 407–423.
Zhang, A.P., Zheng, Y.C., Xu, B., Fu, Q., Ma, W., Wu, C.D., Zhang, C., Shen, Y., Fei, F., 2019. Metallogeny of the Lietinggang-Leqingla Fe-Cu-(Mo)-Pb-Zn polymetallic deposit, evidence from Geochronology, Petrogenesis, and Magmatic oxidation state, Lhasa terrane. Ore Geol. Rev. 106, 318–339.
Zhao, J.X., Qin, K.Z., Li, G.M., Li, J.X., Xiao, B., Chen, L., Yang, Y.H., Li, C., Liu, Y.S., 2014. Collision-related genesis of the Sharang porphyry molybdenum deposit, Tibet: evidence from zircon U-Pb ages, Re-Os ages and Lu–Hf isotopes. Ore Geol. Rev. 56, 312–326.
Zhao, X.Y., Yang, Z.S., Zheng, Y.C., Liu, Y.C., Tian, S.H., Fu, Q., 2015. Geology and genesis of the post-collisional porphyry-skarn deposit at Bangpu, Tibet. Ore Geol. Rev. 70, 486–509.
Zhao, Y.M., Feng, C.Y., Li, D.X., 2017. New progress in prospecting for skarn deposits and spatial-temporal distribution of skarn deposits in China. Miner. Deposits 36, 519–543 in Chinese with English abstract.
Zheng, Y.C., Hou, Z.Q., Gong, Y.L., Liang, W., Sun, Q.Z., Zhang, S., Fu, Q., Huang, K.X., Li, Q.Y., Li, W., 2014. Petrogenesis of Cretaceous adakite-like intrusions of the Gangdese Plutonic Belt, southern Tibet: implications for mid-ocean ridge subduction and crustal growth. Lithos 190, 240–263.
Zheng, Y.C., Fu, Q., Hou, Z.Q., Yang, Z.S., Huang, K.X., Wu, C.D., Sun, Q.Z., 2015. Metallogeny of the northeastern Gangdese Pb-Zn-Ag-Fe-Mo-W polymetallic belt in the Lhasa terrane, southern Tibet. Ore Geol. Rev. 70, 510–532.
Zhou, J.S., Yang, Z.S., Hou, Z.Q., Liu, Y.C., Zhao, X.Y., Zhang, X., Zhao, M., Ma, W., 2017. The geochemical evolution of syncollisional magmatism and the implications for significant magmatic-hydrothermal lead-zinc mineralization (Gangdese, Tibet). Lithos 288–289, 143–155.
Zhu, D.C., Pan, G.T., Chun, S.L., Liao, Z.L., Wang, L.Q., Li, G.M., 2008. SHRIMP zircon age and geochemical constraints on the origin of Early Jurassic volcanic rocks from the Yeba Formation, southern Gangdese in south Tibet. Int. Geol. Rev. 50, 442–471.
Zhu, D.C., Mo, X.X., Niu, Y.L., Zhao, Z.D., Wang, L.Q., Liu, Y.S., Wu, F.Y., 2009. Geochemical investigation of Early Cretaceous igneous rocks along an east-west traverse throughout the central Lhasa terrane. Tibet. Chem. Geol. 268, 298–312.
Zhu, D.C., Mo, X.X., Zhao, Z.D., Niu, Y.L., Wang, L.Q., Chu, Q.H., Pan, G.T., Xu, J.F., Zhou, C.Y., 2010. Presence of Permian extension-and arc-type magmatism in southern Tibet: paleogeographic implications. Geol. Soc. Am. Bull. 122, 979–993.
Zhu, D.C., Zhao, Z.D., Niu, Y.L., Mo, X.X., Chung, S.L., Hou, Z.Q., Wang, L.Q., Wu, F.Y., 2011. The Lhasa terrane: Record of a microcontinent and its histories of drift and growth. Earth Planet. Sci. Lett. 301, 241–255.
Zhu, D.C., Zhao, Z.D., Niu, Y.L., Dilek, Y., Wang, Q., Ji, W.H., Dong, G.C., Sui, Q.L., Liu, Y.F., Yuan, H.L., Mo, X.X., 2012. Cambrian bimodal volcanism in the Lhasa Terrane, southern Tibet: Record of an early Paleozoic Andean-type magmatic arc in the Australian proto-Tethyan margin. Chem. Geol. 328, 290–308.
Zhu, D.C., Zhao, Z.D., Niu, Y., Dilek, Y., Hou, Z.Q., Mo, X.X., 2013. The origin and pre-Cenozoic evolution of the Tibetan Plateau. Gondwana Res. 23, 1429–1454.
Zhu, D.C., Wang, Q., Cawood, P.A., Zhao, Z.D., Mo, X.X., 2017. Raising the Gangdese Mountains in southern Tibet. J. Geophys. Res. Solid Earth 122, 214–223.